國立臺灣大學工學院化學工程學系

碩士論文

Department of Chemical Engineering
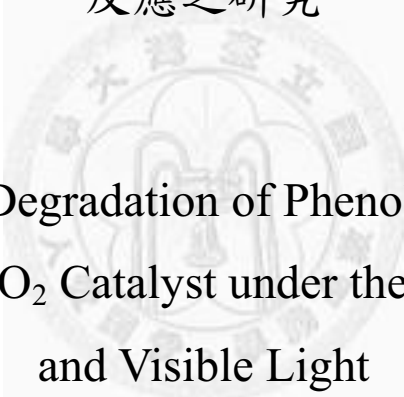
College of Engineering

National Taiwan University

Master Thesis

利用 Au/TiO$_2$ 在紫外及可見光下降解苯酚水溶液的

反應之研究

Photocatalytic Degradation of Phenol Solution in the
Presence of Au/TiO$_2$ Catalyst under the Irradiation of UV
and Visible Light

沈運祥

Yun-Hsiang Shen

指導教授：吳乃立 博士

Advisor: Nae-Lih Wu, Ph.D.

中華民國 100 年 1 月

January, 2011

誌 謝

在實驗室的兩年多日子很快就過去了，這些日子以來，每天都遇到不同的問題，幸好有許多人的幫忙，使我能不斷地朝畢業的目標邁進。

首先最感謝的是指導我完成碩士研究工作的吳乃立教授。教授每天工作的時間比研究生還長，夜晚騎車經過化工館時，二樓西側總有一間辦公室燈火通明。教授對於學生在購買藥品和使用貴儀時，都給予全力支持，從不吝惜於投資大筆經費在做研究方面。此外，教授都以啟發式的教學指導學生循序地找到問題的答案，無形當中培養學生不少解決問題的能力。當然還要感謝萬本儒教授和吳紀聖教授特別在百忙中撥空幫我審查論文與出席學位考試，並且給予我許多研究方法上的指教，使得這本論文的內容能更加完善。

EML 內的許多優秀同學是我學習的好榜樣。首先感謝即將畢業的彥伯和光正學長，每當大多數同學都離開實驗室時，兩位大學長經常還在工綜415 繼續做實驗和寫論文；當大家遇到問題時，兩位大學長也都會很熱心地主動幫忙，帶給大家最好的示範。再來是人氣指數最高的郁婷學姊；產學合作經驗豐富的富生學長；大好人佑展學長；同時精通理論計算和實驗技巧的憲昌學長；EML 內最有品味的崧傑學長；教過我最多東西，同時也是最多才多藝的志毅學長；熱於助人的均潔學姊；文筆豐富的乃璇學姊；實驗室內另一位光觸媒專家嘉男學長；還有與我同居，但是研究成果與課業表現早已超越我甚多的文勤；認真的榮川和維凱間的熱切互動，是團隊合作的最佳示範；實驗數據多到令人嘆為觀止的 Erwin，經常有不少好結果與大家分享；新加入的成員廷育和炯宏，看到你們的進展這麼快，相信

你們的未來一定是前途無量；認真程度不亞於研究生的大四專題生仲琪、彥勛、家邦，在此祝福你們前途似錦。

　　還有，從小到大陪我渡過許多難關，同時一直給予我許多鼓勵和支持我朝既定目標前進的家人，感謝你們讓我能專注地完成學業。最後，謹以這份簡單的著作獻給曾幫助過我的師長與朋友。

運祥　　謹記

庚寅年　暮冬

摘要

　　本研究的目的是想探討利用 Au/TiO$_2$ 對於工業廢水內常見的有機物苯酚進行光催化降解反應，並且觀察中間產物的濃度分佈與選擇性的變化，以及侷域性表面電漿共振 (LSPR) 效應是否可顯著地提升反應速率。

　　本研究分為三大部分。第一部分是用 300 nm 的紫外光源對苯酚的兩種不同的初始濃度 (250 ppm or 150 ppm) 分別進行光催化降解反應，結果發現苯酚的反應速率常數幾乎不受初始濃度影響。第二部分則是探討溫度效應對於 P25 與 2.0 wt% Au/P25 催化活性的影響，我們發現當溫度由 32℃ 上升到 38℃ 時，苯酚的反應速率常數不升反降。之後將反應溫度提高到 55℃ 時，苯酚的反應速率常數也只有略微提升，推測原因可能與吸附步驟是速率決定步驟有關。第三部分是將 300 nm 紫外光與 575 nm 可見光燈管同時打開，觀察 Au/TiO$_2$ 的 LSPR 效應是否會對反應速率造成顯著的影響。結果發現苯酚的反應速率常數有略為提升，中間產物的部分雖然速率常數提升有限，經過與只照可見光的對照組比較，我們覺得 LSPR 效應應該有助於提升反應速率。

關鍵字：二氧化鈦、Au/TiO$_2$、苯酚、光催化降解反應、侷域性表面電漿共振。

Abstract

The purpose of this research is to apply Au/TiO_2 for the photocatalytic degradation reaction of phenol, a commonly found organic compound in industrial wastewater, and to observe the concentration profiles as well as the selectivity of the intermediates. In addition, we want to investigate whether Localized Surface Plasmon Resonance (LSPR) effect can enhance the reaction rate.

This research is divided into three parts. First, we illuminated the phenol solution with 300 nm UV light only. The initial concentration of phenol solution is 250 ppm and 150 ppm, respectively. We found that the reaction rate constant of phenol was nearly independent of the initial concentration. The second part is to explore the temperature effect on the kinetics when using P25 and 2.0 wt% Au/P25 as the catalyst, individually. We observed that when the reaction temperature increased from 32℃ to 38℃, the reaction rate constant of phenol dropped. Even when we elevated the reaction temperature to 55℃, the reaction rate constant of phenol only slightly increased. We suppose that it is because the adsorption step rather than the surface reaction step is the rate-determining step.

The third part is to illuminate the phenol solution with 300 nm UV and 575 nm visible light at the same time. The reaction rate constant of phenol became a little larger when applying dual light sources. As for the mono-hydroxylated intermediates, although the increase in the reaction rate

constant was not obvious, when compared with the data obtained by illuminating the solution with UV light only, we believe that LSPR must promote the overall reaction rate of the photocatalytic degradation reaction of phenol.

Keywords: Titanium dioxide; Au/TiO$_2$; Phenol; Photocatalytic degradation reaction; Localized Surface Plasmon Resonance (LSPR)

Table of Contents

List of Figures

List of Tables

Chapter 1 Introduction

1-1 Background

Treating industrial wastewater has long been a crucial issue, because many kinds of industrial wastewater are non-biodegradable, and contain potential carcinogens [2]. Chemical oxidation, activated carbon adsorption, and biochemical engineering processes are just some of the methods designed to solve this problem. Photocatalytic oxidation is another measure currently gaining attention, because it requires a relatively lower cost than other methods by using only light to initiate the oxidation reaction, which is a green chemical process. Also, if the oxidation reaction is complete, merely carbon dioxide, nitrogen, and water are produced.

1-2 Motivations and Objectives

Among the many photocatalysts discovered, titanium dioxide (TiO_2) still bears the most promising potential to be developed, because it is an inexpensive, non-toxic, and stable material.

However, one of the drawbacks of using TiO_2 is that its band gap energy is 3.2 eV for anatase phase, and 3.0 eV for rutile phase. Namely, the photocatalytic activity of pure TiO_2 does not appear obviously when illuminated by visible light. Several ways have been proposed to reduce the band gap energy of TiO_2 [3]. One promising approach is to load gold atoms on

pure TiO_2 by applying the incipient wetness method [4, 5].

Even if the band gap energy of TiO_2 is narrowed, its photocatalytic activity still has to be examined by some reactions. Many researchers have tried to use different organic dye solutions to test photocatalytic activity [4], such as methyl orange and methylene blue [5]. These are convenient ways to check for the extent of a reaction by detecting the absorption of light of the reactant. But most pollutants in wastewater are aromatic compounds, not those dyes. To address this problem, a phenol solution may be a representative reactant [6]. Phenol is commonly found in industrial wastewater, and its solubility is higher than other aromatic compounds without hydrophilic substituent. I propose that exploring the degradation rate and mechanism of a phenol solution may be the path toward identifying other aromatic compound solutions. Therefore, the objective of this research is to apply Au/TiO_2 to photocatalytic degradation reaction of phenol, and to observe the concentration profiles as well as the selectivity of the intermediates. Also, we want to investigate whether LSPR effect can enhance the reaction rate.

Chapter 2 Literature Review

2-1 An Introduction of Titanium Oxide, TiO_2

Titanium oxide has been a well-known material in semiconductor photocatalysis since Fujishima and Honda discovered the photocatalytic splitting of water on TiO_2 electrodes in 1972 [7]. Since then, there has been a dramatic increase in the number of publications on this promising material, including the fundamental mechanism of photocatalytic reactions and the enhancement of photocatalytic efficiency in the decomposition of environmental pollutants [1, 8, 9]. Among many kinds of heterogeneous photocatalyst, TiO_2-based photocatalysts have drawn much people's attention in the potential application to the total degradation of organic pollutants in air and water [10].

2-1-1 Fundamental Properties

Titanium oxide, a wide band gap and n-type semiconductor, exists in three crystalline forms - anatase, rutile and brookite. The more important crystalline phases are anatase and rutile, which occur in atmosphere and are relatively easier to be prepared [11, 12]. The phase transformation temperature between anatase and rutile is around 600℃, as shown in the phase diagram of TiO_2 (Fig. 2-1) [13].

Both anatase and rutile phase of TiO_2 belong to the tetragonal crystal system. The structures of anatase and rutile phase can be described in terms of

chains of TiO_6 octahedra. The main differences of these two structures are the distortion of each octahedron and the assembly pattern of the octahedra chains, as shown in Fig. 2-2, which reveals the unit cell structures of the anatase and rutile crystals respectively [11]. Each Ti^{4+} is surrounded by an octahedron of six O^{2-} ions. The octahedron in both anatase and rutile phase is not regular, while the former has more orthorhombic distortion than the latter. Therefore, the symmetry of the crystal structure of anatase is much lower than orthorhombic crystal system. For the assembly pattern of the octahedra chains in the anatase structure, each octahedron is in contact with eight neighbors – four sharing an edge and four sharing a corner. On the other hand, in the rutile structure each octahedron is in contact with ten neighbor octahedrons – two sharing edge oxygen pairs and eight sharing corner oxygen atoms. Fig. 2-3 reveals the combination of chains of anatase and rutile phase [14]. Moreover, the distances of Ti-Ti atoms in anatase are greater than those in rutile (3.79 and 3.04 Å for anatase; 3.57 and 2.96 Å for rutile), whereas the Ti-O distances in anatase are shorter than those in rutile (1.934 and 1.980 Å for anatase; 1.949 and 1.980 Å for rutile). These differences in lattice structures result in different mass densities and electronic band structures between anatase and rutile. The difference crystal structures of the two phases are listed in Table 2-1 [12].

Table 2-1. Properties of anatase and rutile phases of TiO_2 [12].

	Anatase	Rutile
Crystal System	Tetragonal	Tetragonal
Lattice constant a	3.78 Å	4.58 Å
Lattice constant c	9.49 Å	2.95 Å
Specific gravity	3.9	4.2
Molar volume	20.156	18.693
Refractive index	2.52	2.71
Permittivity	5.5 – 6.0	6.0 – 7.0
Band gap energy	3.2 eV	3.0 eV
Melting point	Transforms to rutile	1858℃
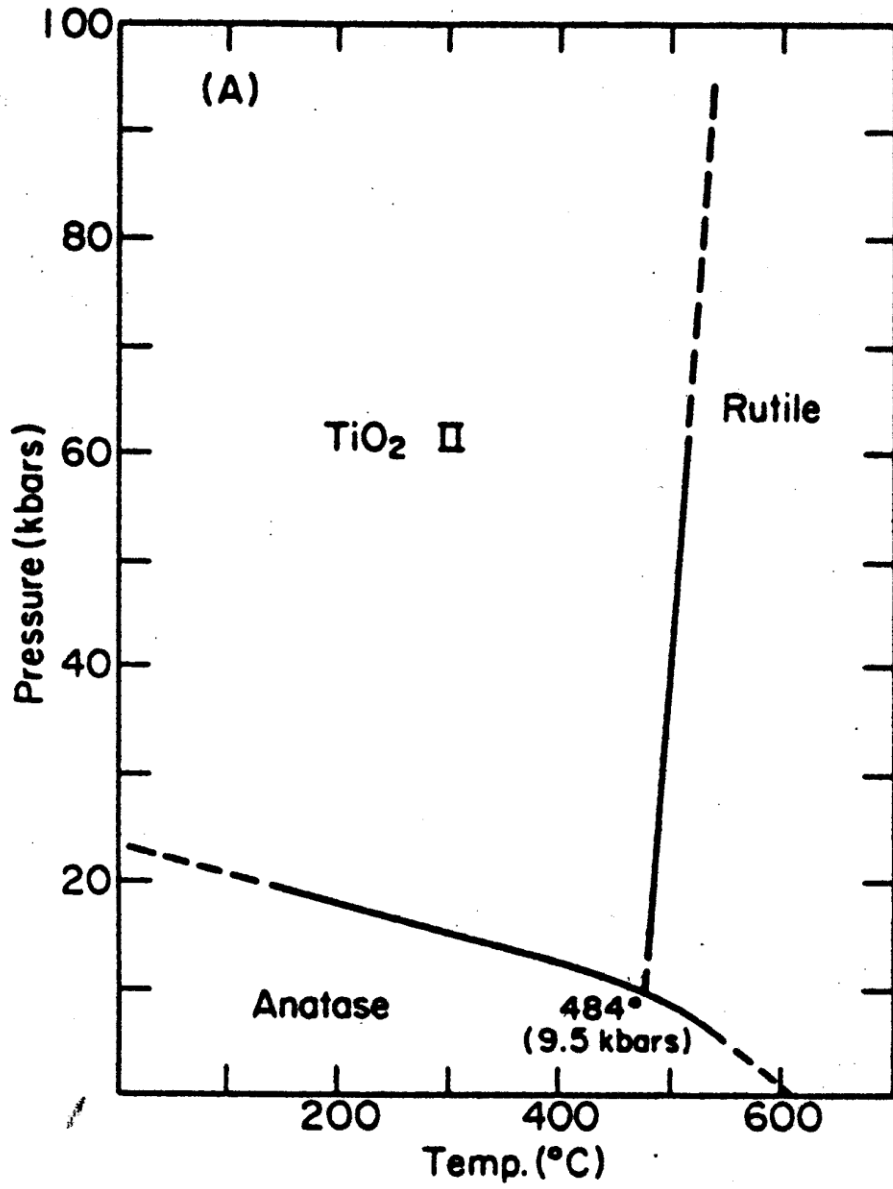
Fig. 2-1. The phase diagram of TiO_2 [13].

(a)
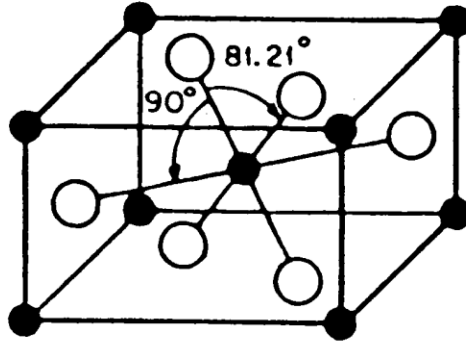
(b)
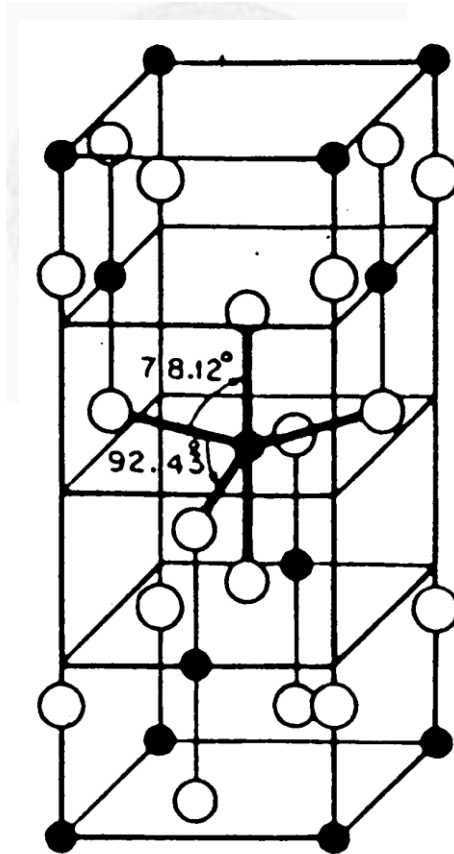
Fig. 2-2. Structures of (a) rutile and (b) anatase [11].
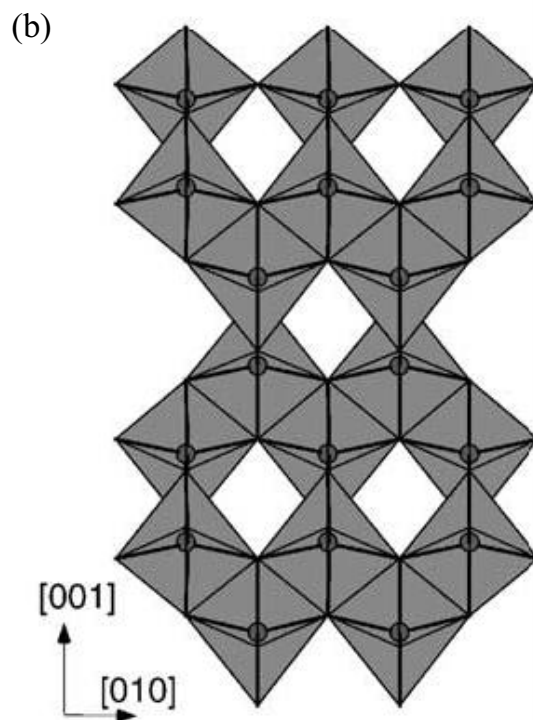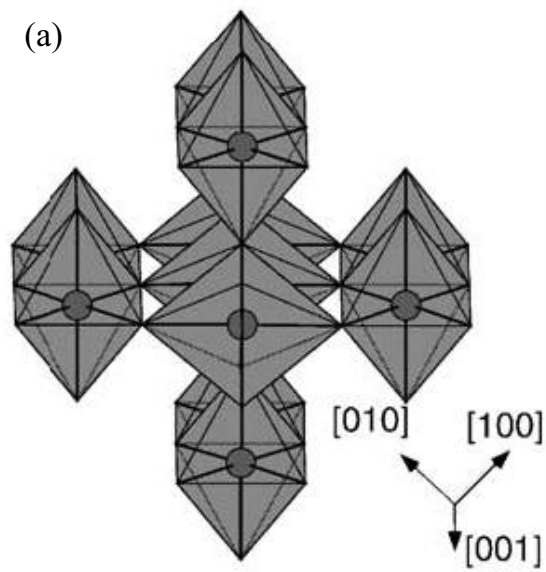
Fig. 2-3. The combination of chains of (a) rutile and (b) anatase [14].

2-1-2 Principles of Photocatalysis

Semiconductors (e.g., TiO_2, ZnO, Fe_2O_3, CdS, and ZnS) can act as sensitizers for light-induced redox processes due to their electronic structures, which are characterized by a filled valence band and an empty conduction band [15]. When a photon with energy of $h\nu$ matches or exceeds the band gap energy, E_g, of the semiconductor, an electron, e_{cb}^-, will be promoted from the valence band (VB) to the conduction band (CB), leaving a hole h_{vb}^+ behind. Once excitation occurs across the band gap, there is a sufficient lifetime, in the nanosecond regime [16], for the created electron-hole pair to undergo charge transfer to adsorbed species on the semiconductor surface. This process is termed heterogeneous photocatalysis if the semiconductor remains intact and the charge transfer to the adsorbed species is continuous and exothermic. The enlarged section of Fig. 2-4 illustrates the excitation of an electron from the valence band to the conduction band initiated by light with energy equal to or greater than the band gap of the semiconductor [11]. Upon excitation, the fate of the separated electron and hole can follow several possible pathways as shown in Fig. 2-4 [17].

The transfer of photoinduced electrons to the adsorbed organic or inorganic species results from migration of electrons and holes to the semiconductor surface, or within the surrounding electrical double layer of the charged particles. The semiconductor can donate electrons to reduce an electron acceptor A on the surface; likewise, a hole can migrate to the surface where an electron from a donor species can combine with it, thus oxidizing the donor species D. The probability and rate of the charge transfer processes for

electrons and holes depend upon the respective positions of the band edges of the conduction and valence bands, as well as on the redox potential levels of the adsorbed species. In competition with charge transfer to the adsorbed species is the recombination electrons and holes. Excited state conduction-band electrons and valence-band holes may recombine in the volume of the semiconductor particle, or on the surface while releasing the input energy as heat.

The band gaps and band edge positions for some ionic and covalent compounds in the bulk state are shown in Fig. 2-5 [18]. The data refer to conditions where the semiconductors are in contact with aqueous redox electrolytes at pH=1, so the internal energy scale given in the left and right side is for comparison with the vacuum level and normal hydrogen electrode (NHE), respectively. Knowing the band positions or flat band potentials is useful because they indicate the thermodynamic limitations of photoreactions to be carried out with the charge carriers. For example, if the reduction of a species in the electrolyte is to occur, the conduction band position of the semiconductor must be higher than the relevant redox level of the species. Generally, anatase phase exhibits higher photocatalytic activity in the degradation of organic pollutants. This could be attributed to two reasons: (1) The band gap of anatase phase (3.2 eV) is greater than that of rutile phase (3.0 eV), so the conduction band edge of anatase must shift to more negative reduction potential, which may enhance the photocatalytic activity. (2) The quantity of OH^- functional groups on the surface of photocatalysts, which has substantial influence on photocatalytic activity, will decrease as temperature increases. Therefore, anatase phase is more practical for environmental applications.
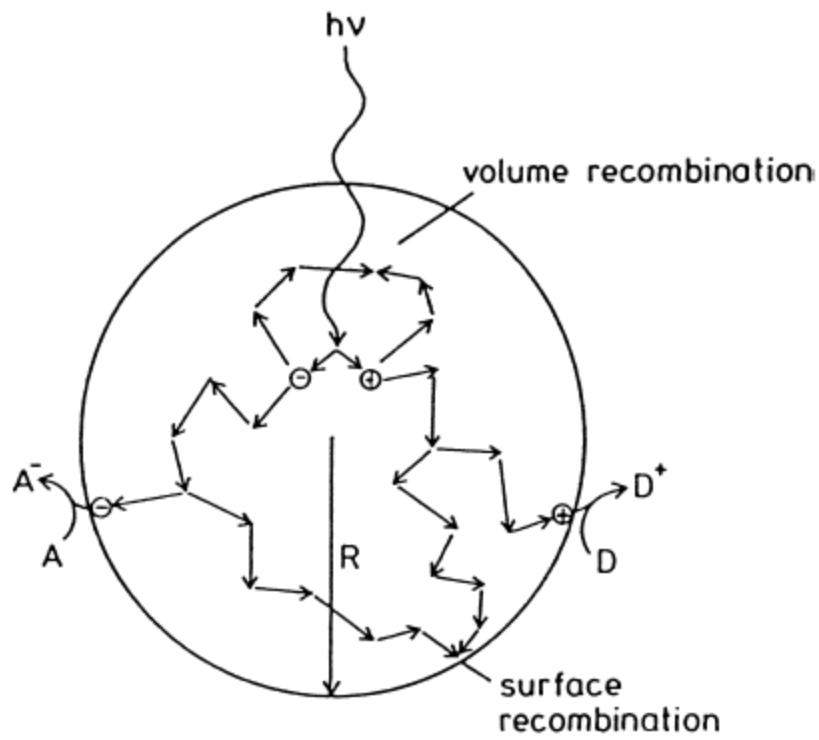
Fig. 2-4. Fate of electrons and holes within a spherical particle of titania in the presence of acceptor (A) and donor (D) molecules [17].
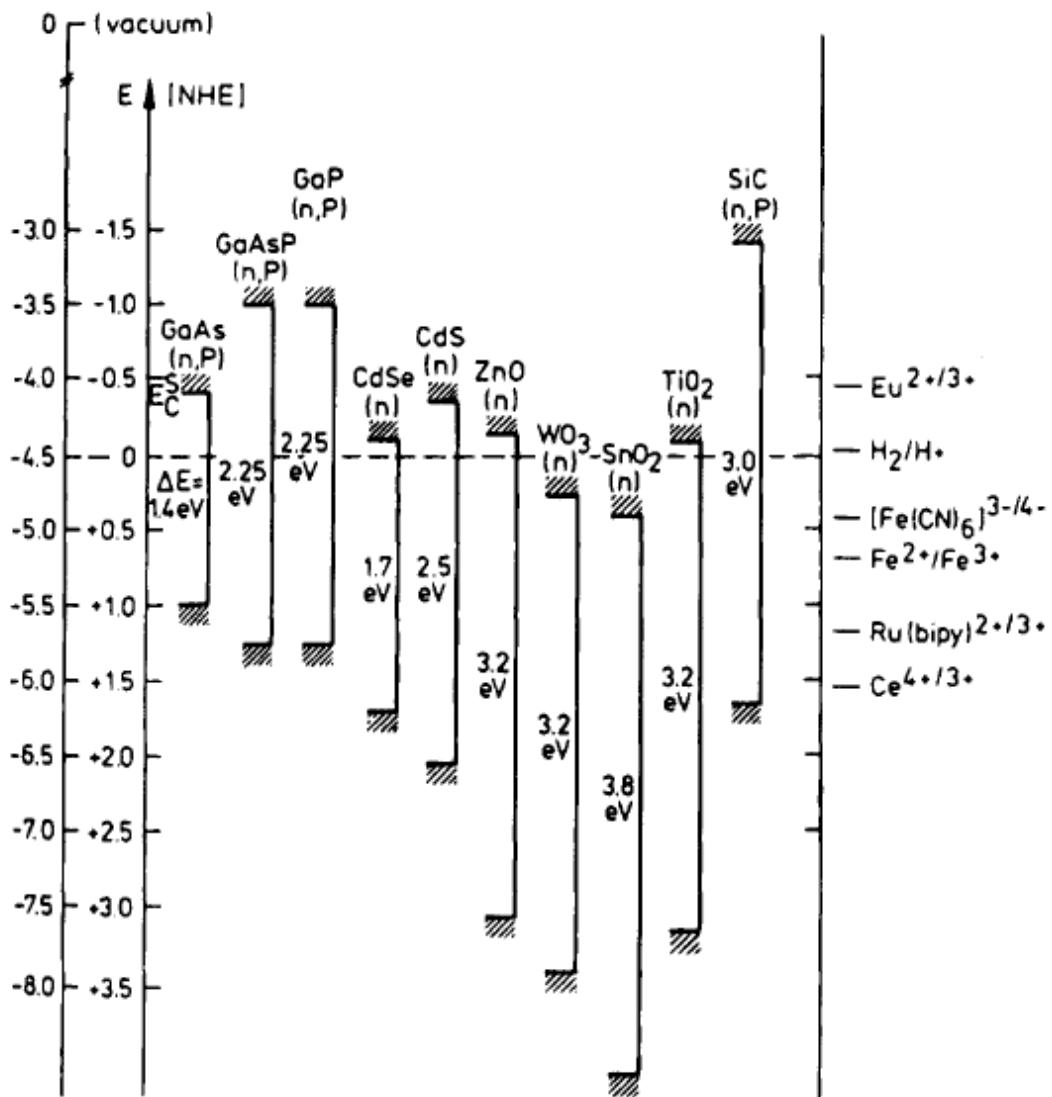
Fig. 2-5. Band edge positions of several semiconductors in contact with aqueous electrolyte at pH=1 [18].

2-1-3 Mechanisms of Photocatalysis

When it comes to the fundamental mechanisms of photocatalysis, several researchers have proposed considerable details of the following general mechanism of heterogeneous photocatalysis on TiO_2 [1, 15, 19], as listed in Table 2-2. Characteristic times for every step in the mechanism are given to the right of each step. >TiOH represents the primary hydrated surface functionality of TiO_2, e_{cb}^- is a conduction-band electron, e_{tr}^- is a trapped conduction-band electron, h_{vb}^+ is a valence-band hole, Red is an electron donor(i.e., reductant), Ox is an electron acceptor (i.e.,oxidant), $\{>Ti^{IV}OH\bullet\}^+$ is the surface-trapped VB hole (i.e., surface-bound hydroxyl radical), and $\{>Ti^{III}OH\}$ is the surface-trapped CB electron. The dynamic equilibrium of equation 1-3a represents the reversible trapping of a conduction-band electron in a shallow trap below the conduction-band edge, since that there is a finite probability that e_{tr}^- may be transferred back into the conduction band at room temperature. Fig. 2-6 schematically illustrates the kinetics of the primary steps in above photoelectrochemical mechanism.

According to the mechanism proposed above, the overall quantum efficiency for interfacial charge transfer is dominated by two critical processes. They are the competition between charge carrier recombination and trapping (picoseconds to nanoseconds), followed by the competition between trapped carrier recombination and interfacial charge transfer (microseconds to milliseconds). Hence, an increase in either the recombination lifetime of charge carriers or the interfacial electron-transfer rate constant is expected, for it must

result in higher quantum efficiencies for steady-state photolysis.

Table 2-2. Primary process and associated characteristic time domains in the TiO$_2$-sensitized photodecomposition of organic pollutants [1].

Primary Process	Characteristic Time	
Charge-carrier generation		
$TiO_2 + hv \rightarrow h_{vb}^+ + e_{cb}^-$	(fs)	(1-1)
Charge-carrier trapping		
$h_{vb}^+ + >Ti^{IV}OH \rightarrow \{>Ti^{IV}OH\bullet\}^+$	fast(10 ns)	(1-2)
$e_{cb}^- + >Ti^{IV}OH \leftrightarrow \{>Ti^{III}OH\}$	Shallow trap (100ps)	(1-3a)
	(dynamic equilibrium)	
$e_{cb}^- + >Ti^{IV} \rightarrow >Ti^{III}$	deep trap (10 ns)	(1-3b)
	(irreversible)	
Charge-carrier recombination		
$e_{cb}^- + \{>Ti^{IV}OH\bullet\}^+ \rightarrow >Ti^{IV}OH$	slow (100 ns)	(1-4)
$h_{vb}^+ + \{>Ti^{III}OH\} \rightarrow Ti^{IV}OH$	fast (10 ns)	(1-5)
Interfacial charge transfer		
$\{>Ti^{IV}OH\bullet\}^+ + Red \rightarrow >Ti^{IV}OH + Red\bullet$	slow (100 ns)	(1-6)
$e_{tr}^- + Ox \rightarrow >Ti^{IV}OH + Ox\bullet^-$	very slow (ms)	(1-7)

Fig. 2-6. Kinetics of the primary steps in photoeletrochemical mechanism [1].

2-1-4 Formation of Hydroxyl Radicals

The formation of hydroxyl radicals (OH·) lies in the existence of light, air, and water. Many mechanisms have been proposed to explain how hydroxyl radicals are formed. The general mechanism is as follows [20]:

$$TiO_2 + h\nu \rightarrow e_{cb}^- + h_{vb}^+ \tag{2-1}$$

$$e_{cb}^- + h_{vb}^+ \rightarrow heat \tag{2-2}$$

$$h_{vb}^+ + H_2O \rightarrow OH\cdot + H^+ \tag{2-3}$$

$$h_{vb}^+ + OH^- \rightarrow OH\cdot \tag{2-4}$$

$$e_{cb}^- + O_2 \rightarrow O_2^- \tag{2-5}$$

$$O_2^{\cdot-} + O_2^{\cdot-} + 2H^+ \rightarrow H_2O_2 + O_2 \tag{2-6}$$

$$O_2^{\cdot-} + H^+ \rightarrow HO_2\cdot \tag{2-7}$$

$$HO_2\cdot + H^+ + e_{cb}^- \rightarrow H_2O_2 \tag{2-8}$$

$$H_2O_2 + h\nu \rightarrow 2\ OH\cdot \tag{2-9}$$

$$H_2O_2 + e_{cb}^- \rightarrow OH\cdot + OH^- \tag{2-10}$$
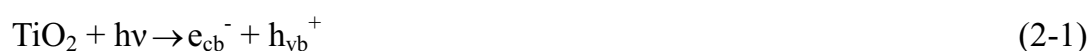
Although other active photooxidants, such as superoxide ions ($O_2^{\cdot-}$), holes (h_{vb}^+), and hydroperoxyl radical ($HO_2\cdot$), also bear the potential to decompose organic pollutants, hydroxyl radicals play a major role in many photocatalytic reactions. Indeed, hydroxyl radicals are known as the second best oxidizing agent after fluorine [17].

The existence of hydroxyl radicals has been proved by adding scavengers, such as methanol, into the solution containing TiO_2. Also, the electron spinning resonance (ESR) spectrum also shows the peaks of hydroxyl radicals [4].
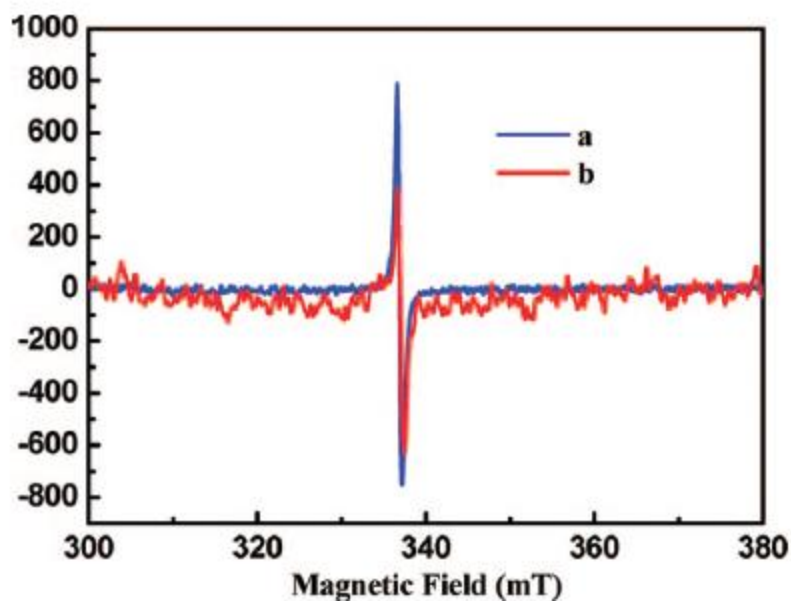
Fig. 2-7. ESR spectrum of (a) H_2TPPC-TiO_2 and (b) TNO_2PP-TiO_2 at room temperature generated after the irradiation of high-pressure mercury lamp [4]. (H_2TPPC: meso-tetra (4-carboxyphenyl) porphyrin, TNO_2PP: meso-tetra (4-nitrophenyl) porphyrin)

2-1-5 Applications of TiO_2 to Photocatalysis

Photocatalysis has received more attention from people since the spread of Severe Acute Respiratory Syndrome (SARS) in 2003. Many commercial products have been advertised to have coated TiO_2 on the surface of them. Among many photocatalysts discovered and researched, TiO_2 is still a famous one and has been commercialized, such as Degussa P25 and Hombikat UV100. This is because TiO_2 bears relative higher photocatalytic activity, stability, and lower cost than its competitors. Fig. 2-8 demonstrates some major applications of TiO_2, and they all have something to do with promoting our living quality [12, 21]. For example, by applying TiO_2 in the water treatment, nearly no other

harmful product is generated after complete reaction. And if CO_2 can further be reduced with another TiO_2-based photocatalytic system, the world would be so wonderful under the operation of these photocatalytic reactions.
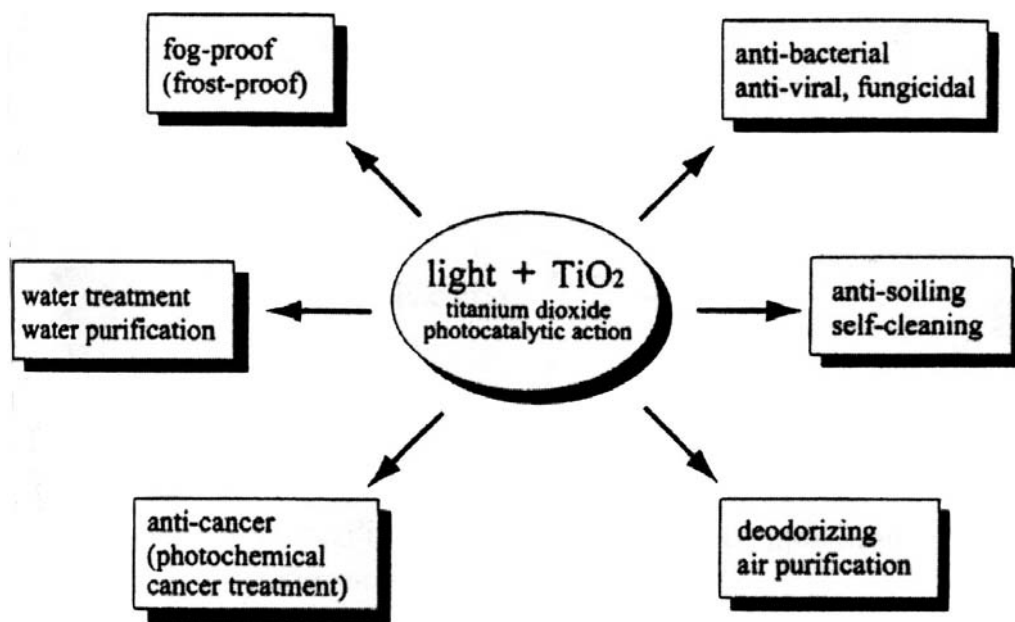
Fig. 2-8. Major applications of TiO_2 photocatalysis [12].

2-2 Photocatalytic Oxidation of Phenol

Among many organic pollutants, phenol is chosen as the model compound for research in this study, because phenol is a useful precursor when synthesizing many organic compounds, such as salicylic acid, anisole, naphthol, etc. The wastewater released from many factories may contain high concentration of phenol or its derivatives. However, according to the regulations set by the Envionmental Protection Administration (EPA), the concentration of phenol in water cannot exceed 1.0 mg/L (1 ppm), or human bodies cannot sustain it. So it is quiet important to monitor the concentration of

phenol in drinking water. Photocatalytic oxidation is one of many ways to eliminate phenol and its derivatives from wastewater.

2-2-1 Comparison of the Toxicity of the Reactant and Intermediates

The median lethal dose (LD_{50}) is a general indicator of a substance's acute toxicity. The following Table 2-3 shows the LD_{50} of phenol and its mono-hydroxylated intermediates. The data are obtained from Registry of Toxic Effects of Chemical Substances (RTECS) and International Uniform Chemical Information Database (IUCLID). We think that the overall toxicity of phenol solution will be reduced after phenol is degraded, because the LD_{50} of phenol is higher than its mono-hydroxylated intermediates.

Table 2-3. Comparison of the median lethal dose.

Chemical	Animal, Route	LD_{50}	Data Source
phenol	rat, oral	317 mg/kg	RTECS
1,2-benzenediol	rat, oral	260 mg/kg	RTECS
1,3-benzenediol	rat, oral	301 mg/kg	RTECS
1,4-benzenediol	rat, oral	302 mg/kg	IUCLID

2-2-2 Effect of Reaction Temperature

Generally speaking, the effect of temperature on reaction rate is important to some extent, since that temperature is a symbol of the kinetic energy of molecules. Arrhenius equation listed in Eq. (2-11) is a typical way to depict the

relationship between reaction temperature and rate constant. When the reaction temperature increases, the molecules with energy more than the activation energy also increase, and that will accelerate the reaction rate. However, for photocatalytic oxidation of organic pollutants, when using TiO_2 as the catalyst, the whole process is not very temperature sensitive. The activation energy of some photocatalytic reactions is listed in Table 2-4 [22]. For example, the heat of chemisorption is about 40 kJ/mol, which is four times larger than the activation energy of photocatalytic oxidation of phenol. Therefore, when the light source is the same, even though the reaction temperature is different about up to 2℃ in each experiment, the temperature might not have too severe impact on the reaction rate constant.

$$k = Ae^{-\frac{E_a}{RT}}$$ (2-1)

where   k   :   reaction rate constant

         A   :   pre-exponential factor

         E_a :   activation energy (kJ/mol)

         R   :   gas constant (kJ/mol*K)

         T   :   absolute temperature (K)

Table 2-1. Activation energy of some photocatalytic reactions [22].

Reactant	TiO$_2$ catalyst	E$_a$ (kJ/mol)	T (K)	Reference
4-chlorophenol	Deposited	20.6	283~333	[23]
4-chlorophenol	Suspension	16.0	288~328	[24]
4-chlorophenol	Suspension	5.5	283~318	[25]
Methyl orange	Suspension	18.0	300~318	[26]
Dichlorvos	Deposited	28.4	293~313	[27]
Malonic acid	Suspension	9.99	294~324	[28]
Phenol	Suspension	10.0	293~323	[29]
Salicylic acid	Deposited	11.0	298~318	[30]
Xylenols	Suspension	8.8	279~333	[31]
4-nitrophenol	Suspension	7.42	288~323	[22]

2-3 Localized Surface Plasmon Resonance (LSPR)

2-3-1 Introduction of LSPR

Localized surface plasmons (LSPs) are charge density oscillations confined to metallic nanoparticles (sometimes referred to as metal clusters) and metallic nanostructures. Exciting LSPs by an electric field (light) at an incident wavelength where resonance occurs will result in strong light scattering in the appearance of intense surface plasmon (SP) absorption bands, and an enhancement of the local electromagnetic fields. The frequency and intensity of the SP absorption bands are characteristic of the material being illuminated (typically, gold, silver, and platinum), and are highly sensitive to the size, size

distribution, shape of the nanostructures, as well as to the environment around them [32, 33]. Fig. 2-1 illustrates how the electron clusters are affected by the incident electromagnetic wave, and the change of Poynting vector around the small aluminum sphere.

Awazu et al. proved that the enhancement of electromagnetic field in the near-UV region can promote the degradation rate of methylene blue by a factor of 7. They hypothesized that because the band gap of anatase phase is 3.26 eV, near-UV irradiation can excite pairs of electrons and holes. Ag nanoparticles (NPs) show a very intense LSP absorption band in the near-UV region. This is associated with a considerable enhancement of the electric near-field in the vicinity of Ag NPs. The excitation of electron-hole pairs in TiO_2 and the efficiency of photocatalysis is therefore boosted, as is shown in Fig. 2-2 [33].
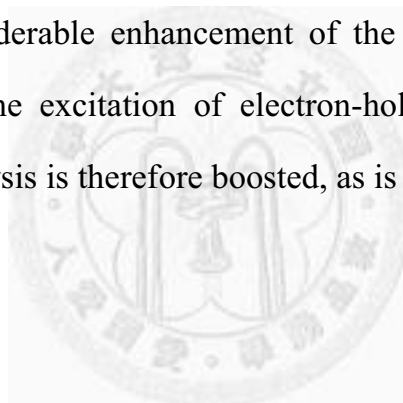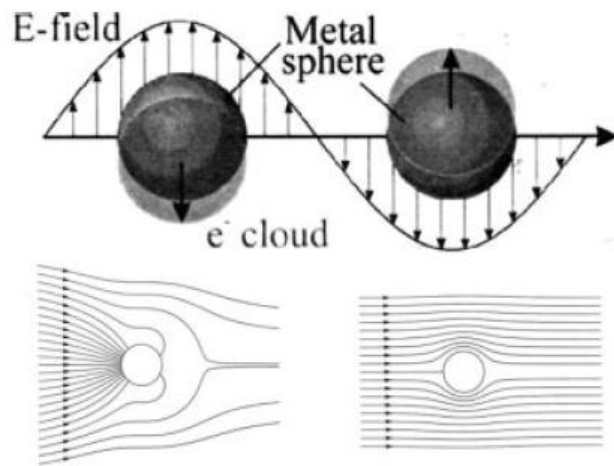
Fig. 2-1. Top: Schematics for plasmon oscillation for a sphere, showing the displacement of the conduction electron charge cloud relative to the nuclei. Bottom: Field lines of the Poynting vector (excluding that scattered) around a small aluminum sphere illuminated by light of energy 8.8 eV where resonance occurs (left hand side) and 5 eV where there is no resonance (right hand side) [32].
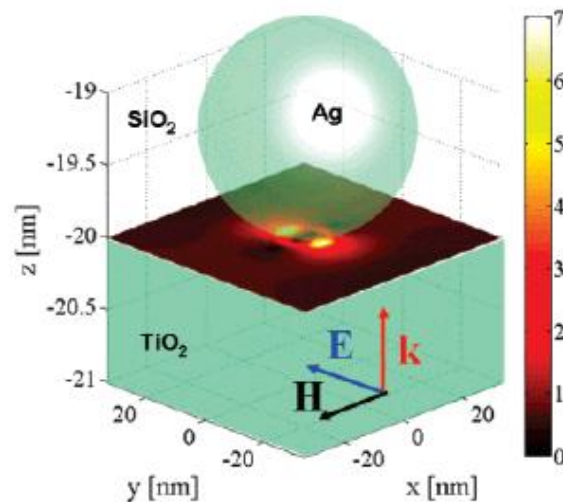
Fig. 2-2. Amplitude enhancement inside a TiO_2 substrate was shown at the interface to a SiO_2 substrate where a Ag NP with a diameter of 40 nm is embedded. The center of the coordinate system coincides with the center of the NP. The sketched sphere does not possess the correct dimensions, but merely serves to indicate the geometrical situation that was simulated [33].

2-3-2 Gold Nanoparticles

Gold has been thought to be an inert material to be used in catalysis; however, in 1987, Haruta et al. discovered that when the size of gold is reduced to less than 10 nm, gold becomes an active material that it can catalyze carbon monoxide to carbon dioxide at room temperature [34]. Afterward, many researchers have tried to find out the catalytic properties of gold, and the conclusion is similar that only when the size of gold is less than 10 nm will it turns into an active material [35, 36]. But when it comes to LSPR phenomenon, the particles with lager size are often desired.

The application of gold has been applied to many reactions, such as the oxidation of carbon monoxide to carbon dioxide, water-gas shift reaction. What makes nanogold so appealing lies in its catalytic activity will appear under mild condition, combined with its relative high selectivity, and relative lower cost than other noble metals, gold nanoparticles do open a new era of their own.

Chapter 3 Experimental

3-1 Chemical Reagents and Experimental Instruments

3-1-1 Chemical Reagents

All the chemical reagents used in the experiments are laboratory grade without any further purification, and they are listed alphabetically in Table 3-1. Moreover, the deionized water used in all of the experiments is purified by a reverse-osmosis system (Purelab Maxima/EGLA), the resistivity of which is 18.2 MΩ-cm.

Table 3-1. The chemicals used in this study.

Chemical Reagent	Formula	Assay	Company
Acetonitrile	CH_3CN	99.9%	Merck
Catechol (1,2-benzenediol)	$C_6H_4(OH)_2$	99%	Acros
Ethanol	C_2H_5OH	95%	Taiwan tobacco and liquid corporation
Hydrogen tetrachloroaurate (Ⅲ) trihydrate	$HAuCl_4 \cdot 3H_2O$	-	Acros

Hydroquinone (1,4-benzenediol)	$C_6H_4(OH)_2$	99.5%	Acros
Methanol	CH_3OH	99.9%	Mallinckrodt
Phenol	C_6H_5OH	98.5%	Showa
Phosphoric acid	H_3PO_4	85.8%	J.T.Baker
Potassium phosphate	KH_2PO_4	99%	Acros
Resorcinol (1,3-benzenediol)	$C_6H_4(OH)_2$	98%	Acros
Sodium bisulfite	$NaHSO_3$	95% (w/w)	Showa
Titanium dioxide (P25)	TiO_2	-	Frankfurt
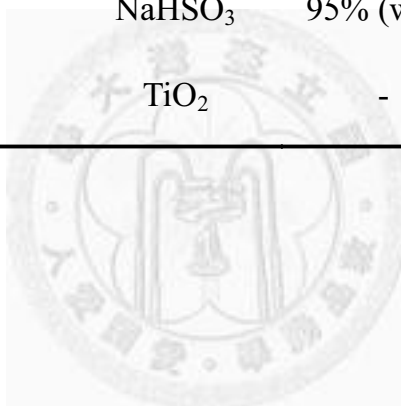
3-1-2 Experimental Instruments

The analytical instruments used to analyze the samples are listed alphabetically in Table 3-2.

Table 3-2. Analytical instruments.

Technique of Analysis	Instrument Model	Supplier
High-performance Liquid Chromatography (HPLC)	Series 200	PerkinElmer
Transmission Electron Microscopy (TEM)	H-7100	Hitachi
High-resolution Transmission Electron Microscopy (HRTEM)	Tecnai G2	Philips
UV-Visible Spectrometer (UV-Vis)	Cary 100 Conc	Varian
X-ray Diffraction (XRD)	X'pert	Philips

Some essential equipment used in the process of experiments is also listed alphabetically in Table 3-3.

Table 3-3. Essential equipment.

Apparatus	Instrument Model	Supplier
Centrifuge	CN-1040	Hsiangtai
Photochemical Reactor	RPR-100	Rayonet
Ultrasonic Cleanser	5510	Branson

3-2 Photocatalytic Reaction

3-2-1 Preparation of Gold Catalysts

All the gold catalysts used in the photocatalytic degradation of phenol solution were prepared by incipient wetness method.

At first, 0.1 M $HAuCl_{4(aq)}$ was prepared under the dark surrounding. 1.5 g TiO_2 (P25) was placed in the agate mortar, and then 1.5 mL of 0.1 M $HAuCl_{4(aq)}$ was added into the mortar drop by drop. At the same time, P25 in the mortar was mixed with $HAuCl_{4(aq)}$ rigorously by using an agate pestle. After 1.5 mL $HAuCl_{4(aq)}$ was all added on P25, the surface of P25 became slightly wet.

The slurry was moved to an alumina boat before calcination. The calcination condition under the flow rate of air at 0.4 L/min was as follows: Increased the temperature in the oven at the rate of 300℃/hr, and the maximum temperature was set to be 300℃ and maintained for 3 hours. Afterward, the temperature decreased naturally to room temperature. 2.0 wt% Au/P25 powder was obtained after grinding the calcined bulky Au/P25.

1.0 wt% and 0.5 wt% Au/P25 were prepared in a similar way, except that the concentration of $HAuCl_{4(aq)}$ was diluted. Also, because the surface property of P25 would change after treated with acidic solution, the HCl-P25 catalyst was prepared after treating 1.5 g P25 with 1.5 mL $HCl_{(aq)}$ (pH=1.67), and the further calcination condition was the same as before.
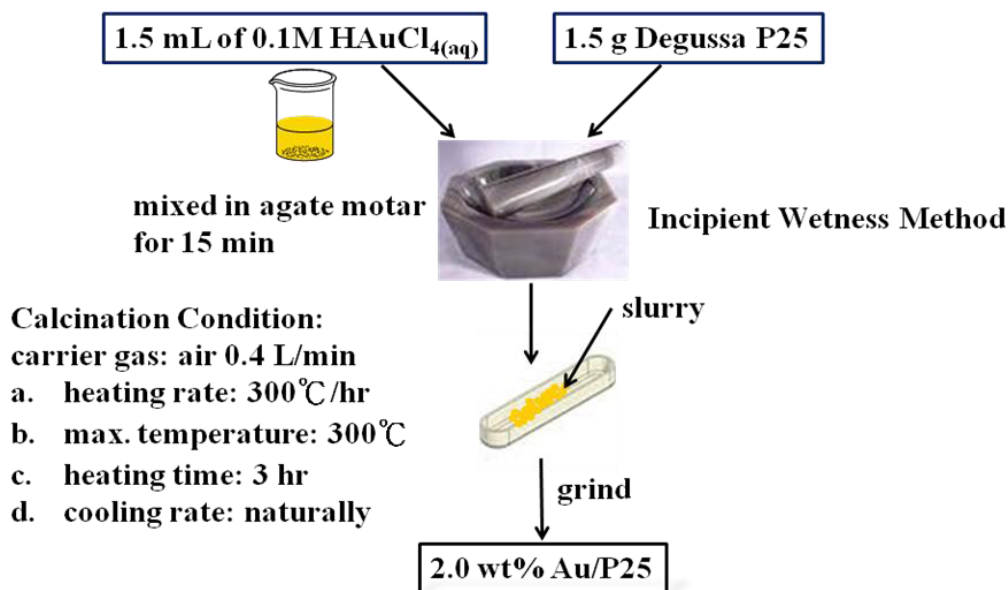
Fig. 3-1. Flowchart of synthesizing Au/TiO$_2$ by incipient wetness method.

3-2-2 Schema of Photochemical Reactor

The top-side view of photochemical batch reactor is shown in Fig. 3-2. A quartz beaker is placed in the center of the reactor, and there is a cooling fan under the magnetic stirrer to remove the heat generated after the light is turned on. Up to 16 light tubes can be placed around the quartz beaker symmetrically, and the power of each tube is 13 W. A thermocouple is placed in the solution to monitor the temperature change during the process of reaction; moreover, when there is a need to increase the reaction temperature, a heating tube with diameter of 11 mm can be place into the solution at the same time. Since that both the thermocouple and heating tube are connected to a PID temperature controller, the temperature is monitored and adjusted to the set value all the time when the heating tube is immersed in the solution. Also, the top of the quartz beaker is covered with handi-wrap to prevent the solution from being

vaporized. The perspective drawing of the reactor is shown in Fig. 3-3.

The experimental procedures are explained as follows: 200 mL phenol solution with desired initial concentration, 250 ppm or 150 ppm, was prepared and added into the quartz beaker. 0.08 g catalyst was added into the phenol solution afterward. The whole solution was stirred for about 10 minutes to reach adsorption equilibrium before reaction. After that, the light tubes were turned on. 2 mL samples were taken out by plastic droppers after a period of time. The samples were then centrifuged at 4000 rpm for 10 minutes to remove most of the particles, followed by being filtered through syringe filters. The membrane of the syringe filter is made of polyvinylidene fluoride (PVDF), and its pore size is 0.45 μm. (Pall) Finally, the samples were injected into HPLC-UV to detect the concentration of phenol and its mono-hydroxylated intermediates.

Fig. 3-2. Top-side view of photocatalytic batch reactor.
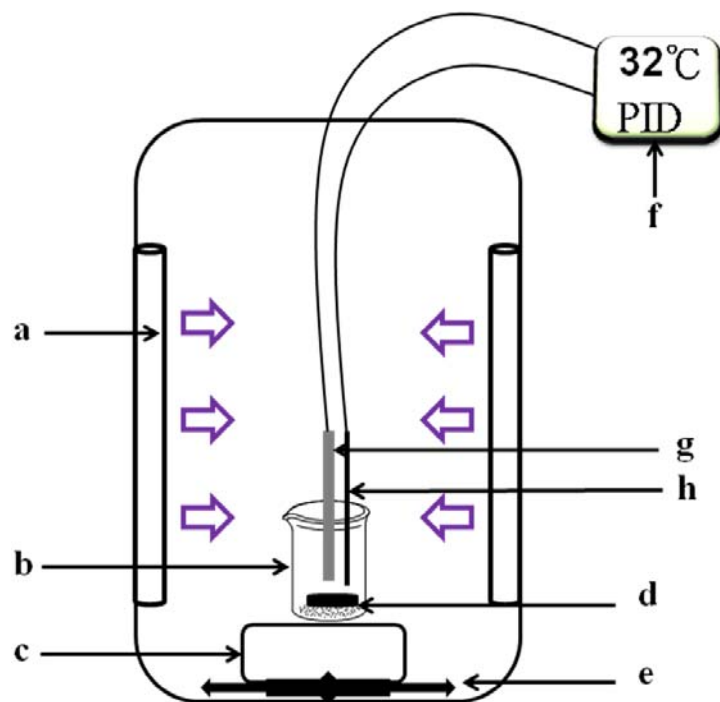
Fig. 3-3. A perspective drawing of the photocatalytic batch reactor. (a) Light tubes (b) 200 mL Quartz beaker (c) Magnetic stirrer (d) Magnetic stirring bar (e) Cooling fan (f) PID temperature controller (g) Heating tube (h) Thermocouple.

3-2-3 Fundamental Experiments

The purpose of this experiment is to explore the kinetics and selectivity of photocatalytic oxidation of phenol, and also to investigate the LSPR effect on the enhancement of the reaction rate. Several independent parameters that may influence the reaction rate will be investigated and discussed here.

<u>Visible Light Effect</u>

Two different light sources were applied in this research, only 300 nm tubes or the combination of 300 nm and 575 nm tubes.

The Amount of Gold Loaded on P25

Three different amounts of gold loaded on P25 were used in the same reaction; that is, 0.5 wt%, 1.0 wt%, and 2.0 wt% Au/P25.

Temperature Effect

When turning UV and visible light tubes on simultaneously, the temperature increased about 6~8℃ compared with that of turning UV light tubes on only. So we selected four different temperatures (32℃, 38℃, 45℃, and 55℃) trying to realize how much did the temperature affect the reaction kinetics. The light source was 8 300 nm UV light tubes, and the initial concentration was 150 ppm.

Initial Concentration

Two different initial concentrations of phenol solution, 250 ppm and 150 ppm, were chosen to compare their effect on reaction kinetics.
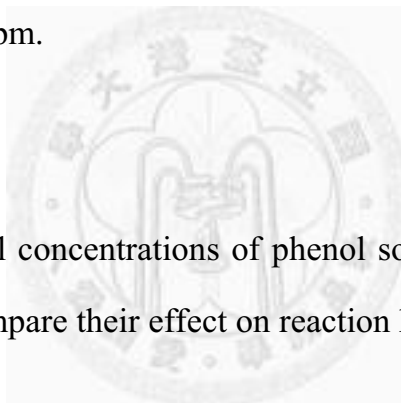
3-3 Analyses and Characterization

3-3-1 X-ray Diffraction (XRD)

XRD was employed here to determine the crystalline phases and identify the existence of gold. Cu-Kα excitation (λ=1.54184 Å) was used as the X-ray generating source, and the applying voltage and current were 45 kV and 40 mA, respectively. All samples were continuously scanned from 2θ equaling 20° to 80°, and the scanning rate was set to be 4.8°/min. The spectra obtained were then compared with the standard spectra in JCPDS 2002.

The crystalline size of TiO_2 was checked by applying Debye-Scherrer's equation shown below, and was further compared with HRTEM micrograph.

$$d = \frac{0.9 \times \lambda}{\left(A^2 - B^2 \right)^{0.5} \cos\theta}$$
(3-1)

where   d   :   Average crystal size

θ   :   Bragg angle

λ   :   X-ray wavelength

A   :   The full width at half maximum (FWHM) of the reflection

B   :   FWHM due to instrument broadening

3-3-2 High-resolution Transmission Electron Microscopy (HRTEM)

The existence and size of gold atoms on P25 were further checked by HRTEM. Small amounts of samples were dispersed in alcohol, and ultrasonically oscillated for about 30 minutes. Then a drop of sample was dropped on a carbon-coated copper grid. The existence of gold was proofed by Energy-dispersive X-ray Spectroscopy (EDX) equipped with HRTEM. In addition, the crystal size of gold was determined by comparing the dimension in the TEM graph with the scale bar in that graph.

3-3-3 UV-Vis Spectrophotometer (UV-Vis)

Deuterium lamps were used as the light source, and the scanning range was from 200 to 800 nm at the rate of 120 nm/min. The powder was filled in a stainless cell and the side facing the light source was transparent, so the samples was tested as if it had been a thin film. The absorption of barium sulfate, $BaSO_4$, was tested first and set as the background value. The Kubelka-Munk (K-M) equation shown below was applied during the measurement of the absorption and scattering of our samples.

$$F(R) = \frac{(1-R_\infty)^2}{2R_\infty} = \frac{K}{S}$$
(3-2)

where   K : absorption coefficient

S : scattering coefficient

R_∞ : limited value of the absolute reflectance

The R$_\infty$ represents the ratio of the diffuse reflectance of our samples (assumed to be infinite thick) to that of a material with high reflectance. The plot of F(R) vs. selected wavelength region will form an absorption spectrum. The absorption spectra did show obvious difference in the visible light region between gold catalysts and pure P25.

3-3-4 High-performance Liquid Chromatography (HPLC)

One of the benefits of HPLC is that it can separate compounds with high boiling point at room temperature. Also, aromatic compounds bear resonance structures, which are favored by using a UV detector to detect their existence. In this research, phenol and its mono-hydroxylated derivatives, the boiling point of which are all above 180℃, were analyzed by the HPLC-UV system. Isocratic elution was carried out with a mixture of 20/80 acetonitrile/phosphate buffer solution (25 mM total phosphate, pH=2.0), and the flow rate was 1.0 mL/min. The column used was a Supelco 516 C-18 (250 mm long×4.6 mm i.d., 5 μm). Detection wavelength was set as 210 nm through the entire analysis process. Before injecting into the column, the mobile phase was filtered through Supelco Nylon 66 membranes (0.45 μm) [37].

3-3-5 Kinetic Analyses

Since that the area under the UV spectra peak is proportional to the concentration of the corresponding compound. To measure the concentration of phenol and its mono-hydroxylated derivatives, four calibration lines were pre-established individually. For phenol, a cup of 300 ppm solution was prepared first, and then it was diluted to 200 ppm, 150 ppm, 100 ppm, 50 ppm,

25 ppm for further analyses by using a 100-1000 μL pipet (eppendorf). Similarly, for 1,4-benzenediol (hydroquinone) and 1,2-benzenediol (catechol), two cups of 60 ppm solution were prepared first, and their concentrations were diluted to 30 ppm, 15 ppm, and 5 ppm afterward. Since that 1,4-benzenediol is not very stable in water, adding 0.15 wt% sodium bisulfite ($NaHSO_3$) as the oxidizing agent into water before preparing standard solution was performed. In addition, because the amount of 1,3-benzenediol (resorcinol) formed was minor than 1,4-benzenediol and 1,3-benzenediol, the calibration line was established at lower concentration, that is, 10 ppm, 5 ppm, 2.5 ppm, and 1 ppm.

When there was only pure water in the sample, no absorption signal was detected under the selected analysis condition, so the calibration lines in Fig. 3-6 and Fig. 3-7 all pass through the origin. Also, the error bars in the figures were plotted after calculating the standard deviation of each data point.
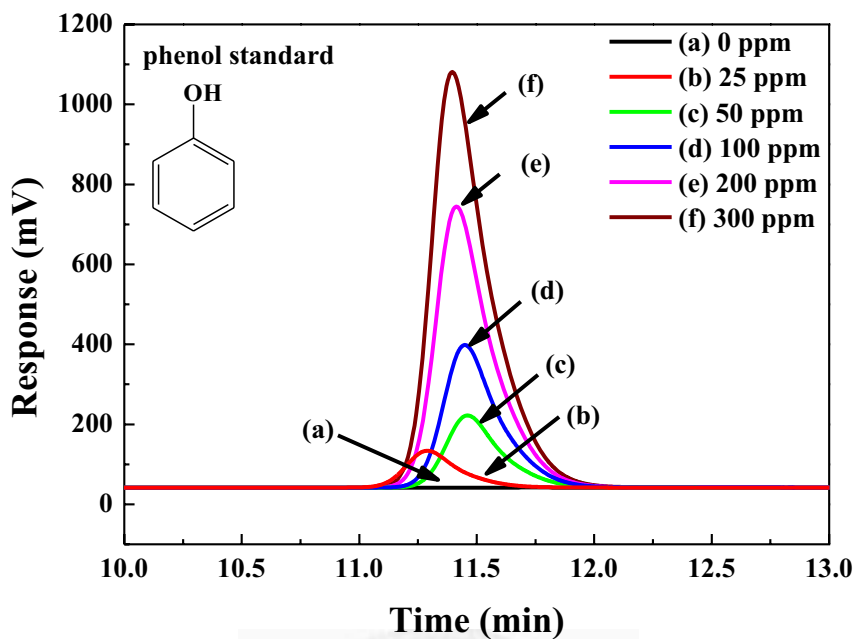
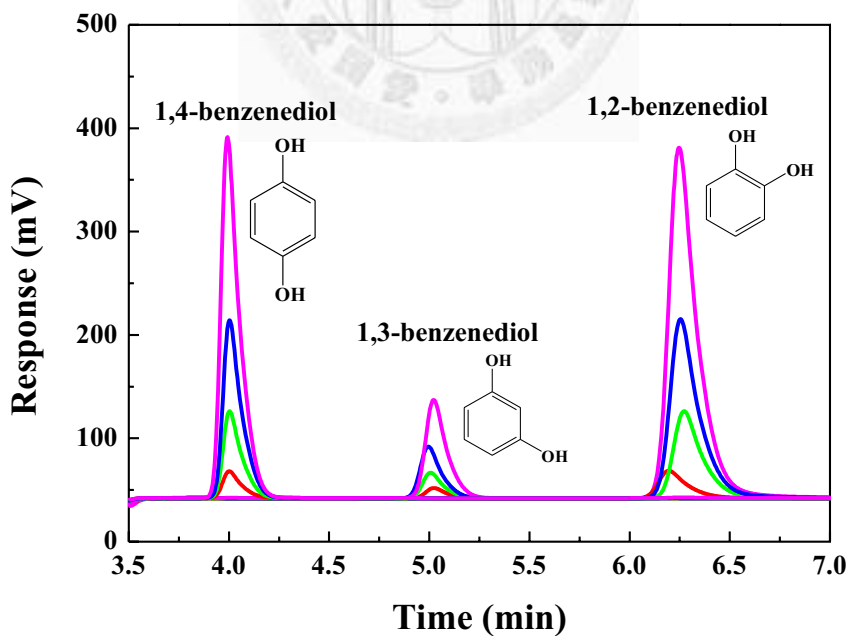Fig. 3-4. Original LC-UV spectra of phenol standards.

Fig. 3-5. Original LC-UV spectra of 1,2-benzenediol, 1,3-benzenediol, and 1,4-benzenediol.
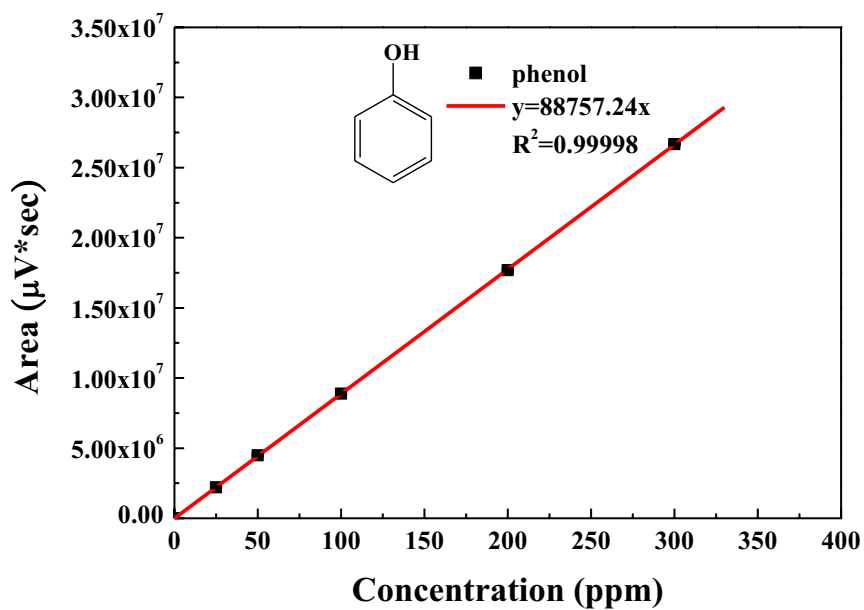
Fig. 3-6. Calibration line of phenol from 0 ppm to 300 ppm.
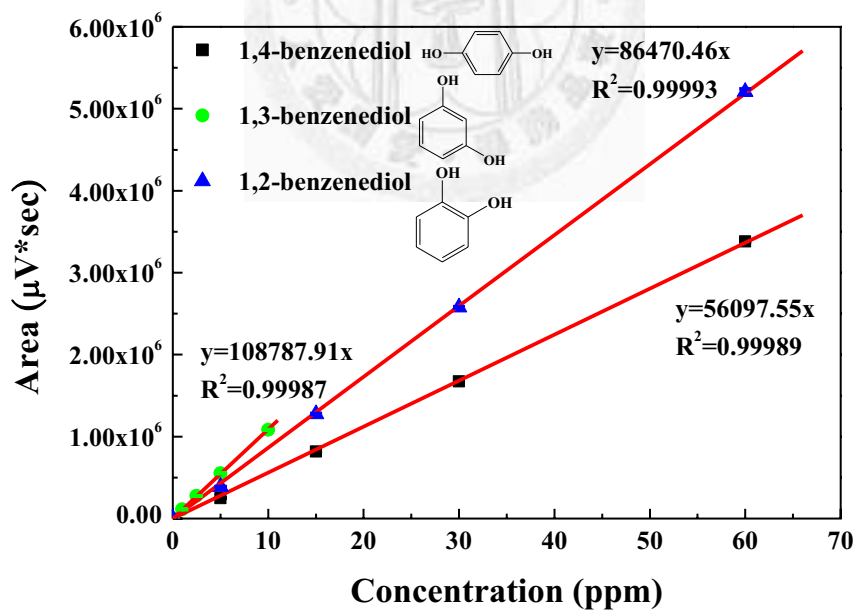
Fig. 3-7. Calibration lines of 1,2-benzenediol, 1,3-benzenediol, and 1,4-benzenediol.

3-3-6 Solving ODEs with 4th-Order Runge-Kutta Method

Runge-Kutta method of order 4 is a well-known multistep method to solve initial value problems. Its formulas are as follows:

$$x(t+h) = x(t) + \frac{1}{6}(K_1 + 2K_2 + 2K_3 + K_4) \tag{3-3}$$

where
$$\begin{cases} K_1 = h \times f(t, x) \\ K_2 = h \times f(t + \frac{1}{2}h, x + \frac{1}{2}K_1) \\ K_3 = h \times f(t + \frac{1}{2}h, x + \frac{1}{2}K_2) \\ K_4 = h \times f(t + h, x + K_3) \end{cases}$$

Here we assume that $f(t,x)$ can be evaluated at any point (t,x). The solution at $x(t+h)$ is obtained at the expense of evaluating f four times per step. This method can be applied to systems of ODE, and x, K, f will be transformed from scalars to vectors with n components. The matrix form of 4th-order Runge-Kutta method is listed as follows:

$$\mathbf{X}(t+h) = \mathbf{X}(t) + \frac{h}{6}(\mathbf{K}_1 + 2\mathbf{K}_2 + 2\mathbf{K}_3 + \mathbf{K}_4) \tag{3-4}$$

where
$$\begin{cases} \mathbf{K}_1 = \mathbf{F}(t, \mathbf{X}) \\ \mathbf{K}_2 = \mathbf{F}(t + \frac{1}{2}h, \mathbf{X} + \frac{1}{2}h\mathbf{K}_1) \\ \mathbf{K}_3 = \mathbf{F}(t + \frac{1}{2}h, \mathbf{X} + \frac{1}{2}h\mathbf{K}_2) \\ \mathbf{K}_4 = \mathbf{F}(t + h, \mathbf{X} + h\mathbf{K}_3) \end{cases}$$

Chapter 4 Results and Discussion

4-1 Characterization of Gold on P25

4-1-1 XRD Analyses

Fig. 4-1 shows the XRD spectrum of Au/P25, HCl-P25, and pure P25. The peaks of anatase and rutile phase can be identified obviously; however, the peaks of gold atoms overlap or are so close with those two phases, and only when 2θ equals about 44.4˚ can we have more chances to identify the existence of gold. The intensity of gold peak increases when the amount of gold increases, but this result may imply that the average particle size also increases when the weight percent of gold on P25 increases. Maybe it is the higher concentration of $HAuCl_{4(aq)}$ when preparing higher weight percent of gold on P25 that causes the agglomeration of gold atoms.

Also, there is no change in the phase types of P25 after being calcined under the same condition as gold catalysts, which might indicate that P25 is quite stable even after being calcined for 3 hours at 300℃.
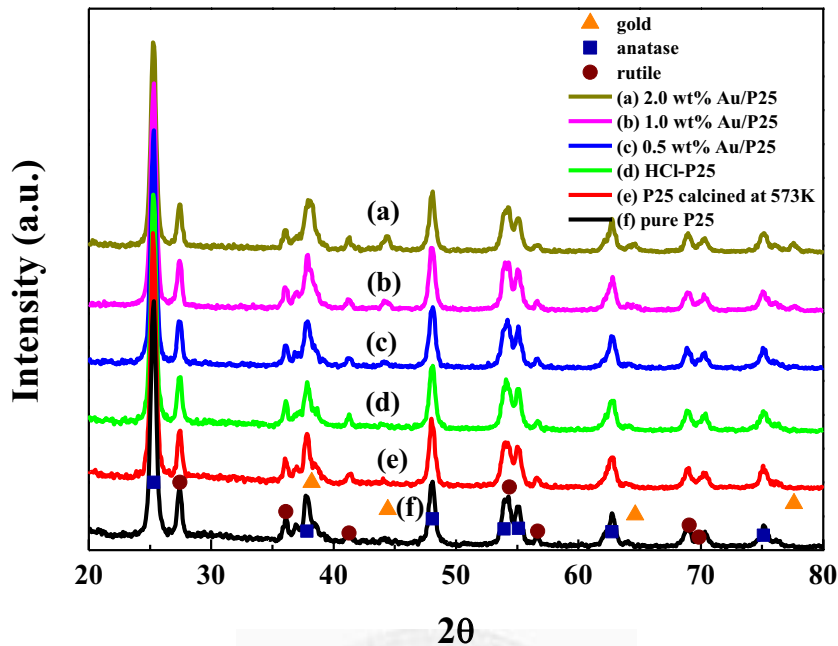
Fig. 4-1. XRD spectrum of P25 and Au/P25.

4-1-2 UV-Vis Analyses

For pure P25 and pure P25 calcined at 300℃, there is only one peak at about 325 nm. But for P25 loaded with gold atoms, another peak at about 560 nm appears, which may be the symbol of Localized Surface Plasmon Resonance (LSPR) phenomenon, as well as the existence of gold on P25. With the increase of gold loaded on P25, the intensity of absorption peaks also increases, but the height of peaks is not proportional to the weight percent of loaded gold. Moreover, the position of LSPR peaks does shift a little to the visible light region as the weight percent of gold on P25 increases, which may demonstrate that the average particle size of gold becomes larger.

The evidence of interband absorption is also shown in Fig. 4-2, because

the absorption intensity of gold catalysts at about 325 nm is stronger than pure P25. This phenomenon is related to the transition of an electron from the occupied d-level to an empty state in the conduction band, the position of which is above the Fermi level in noble metals [38].
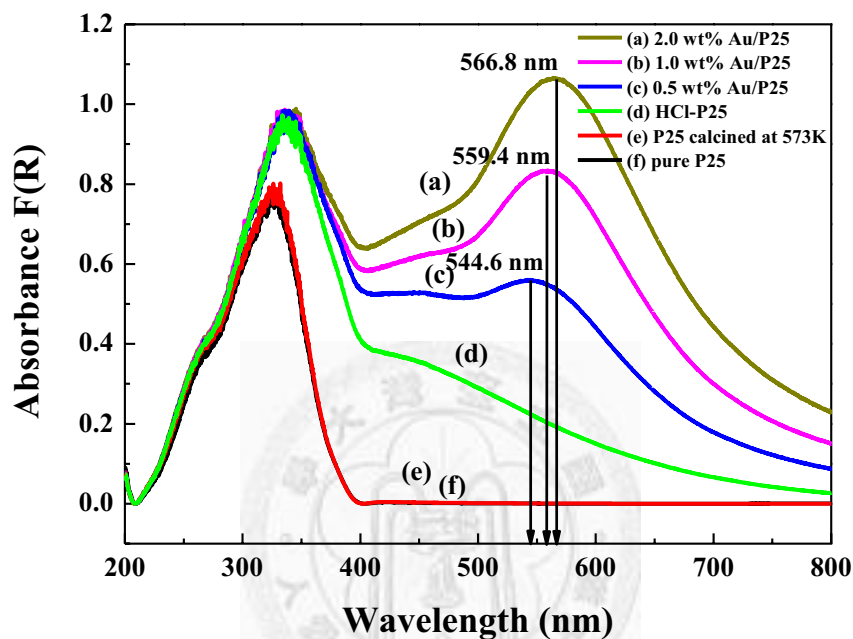
Fig. 4-2. UV-Vis spectrum of P25 and Au/P25.

4-1-3 TEM Analyses

For 2.0 wt% Au/P25, the LSPR peak position obtained from UV-Vis spectrum and Mieplot simulation is quite close, and the particle size set before simulation is close to what we observe in Fig. 4-3 (c). However, for 0.5 wt% Au/P25, if we adopt the data of LSPR peak position of 0.5 wt% Au/P25 in Fig. 4-2, the average particle size of gold should be less than 5 nm from Mieplot simulation. But the TEM image in Fig. 4-3 (e) did not prove our expectation. Perhaps the reason is that Mieplot simulation is suitable for samples with

strong LSPR effects, and the validity of the simulation results will deviate from the true value for samples with weaker LSPR effects. Another reason is that we did not take enough TEM pictures, the gold atoms we saw did not represent the average particle size of gold in the sample. Furthermore, the particle size of P25 remained nearly the same after loading gold on it, which was also checked with XRD spectrum by applying Debye-Scherrer's equation. But the morphology of P25 is destroyed to some extent after treated with acidic $HAuCl_{4(aq)}$, which may affect the photocatalytic activity of P25 itself.

Fig. 4-3. TEM micrographs of P25 and Au/P25 (a) pure P25, (b) HCl-P25, (c) 2.0 wt% Au/P25, (d) EDX spectrum of (c), (e) 0.5 wt% Au/P25, (f) EDX spectrum of (e).
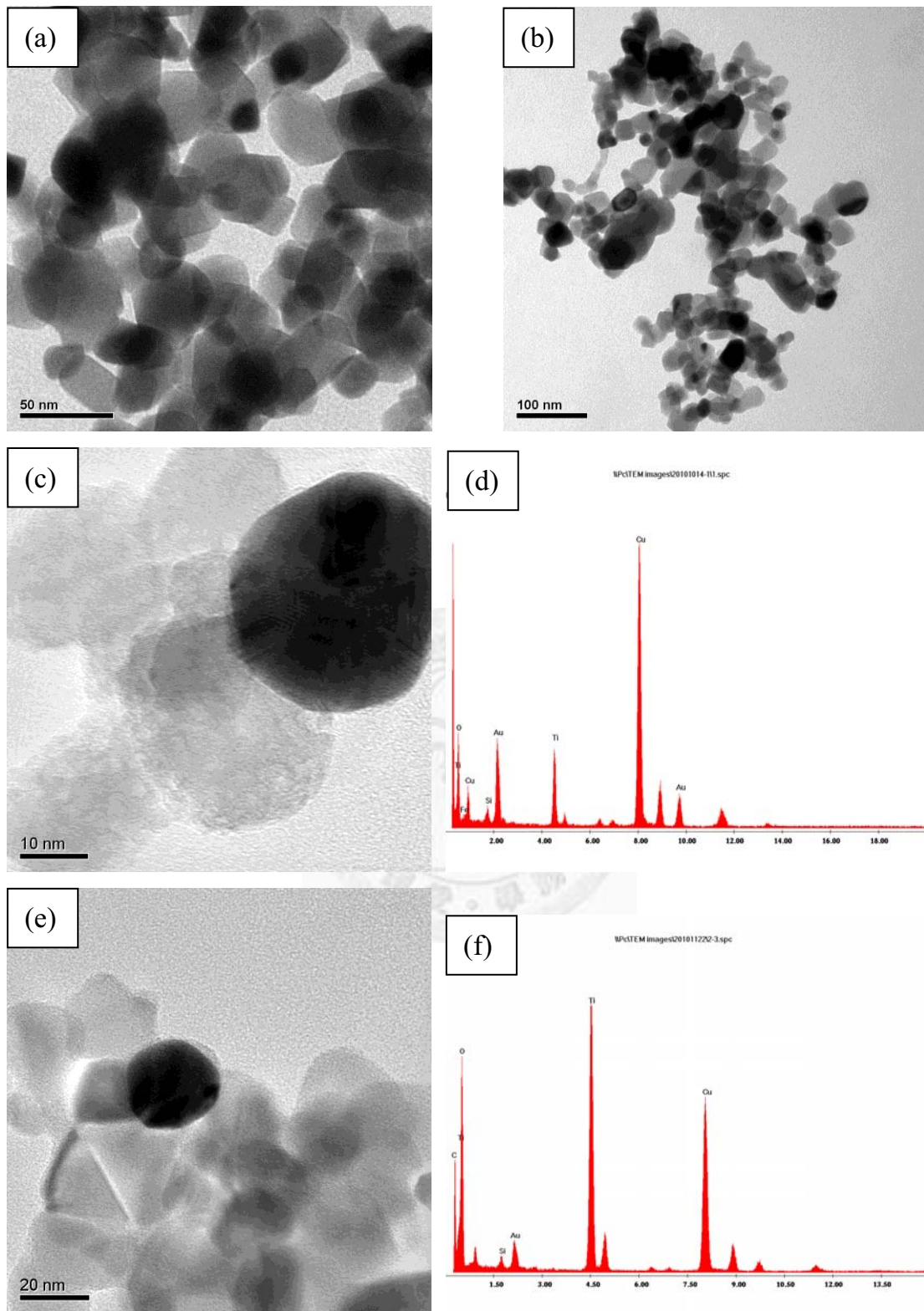
4-1-4 Mieplot Simulation

To further investigate the LSPR phenomenon of metallic nanoparticles, Mieplot computer program was utilized to simulate the extinction and scattering of light from a sphere, and the theory applied is based on Mie theory. Only a gold sphere existed, and the refractive index (RI) of the surrounding medium was tuned from 1.5 to 2.5. As shown in Fig. 4-4, when illuminated by plane wave, the position of LSPR peaks shifts toward visible light region as the particle size of gold increases. The RI value of anatase and rutile phase is 2.5 and 2.9, respectively, but the simulated results cannot match the experimental data when setting the RI equal 2.5 or 2.9; however, if the RI was tuned to 1.75, as the radius of the gold sphere is about 15nm, the peak position is almost the same as that of the experimental data in TEM micrograph (Fig. 4-3 (c)). The proposed reason is that gold atoms are surrounded by P25, but perhaps some parts of the particles are exposed to air, the average RI value of the medium around the particles may be less than 2.5.

Fig. 4-5 demonstrates the relationship between the position of LSPR peak and the particle size of gold.
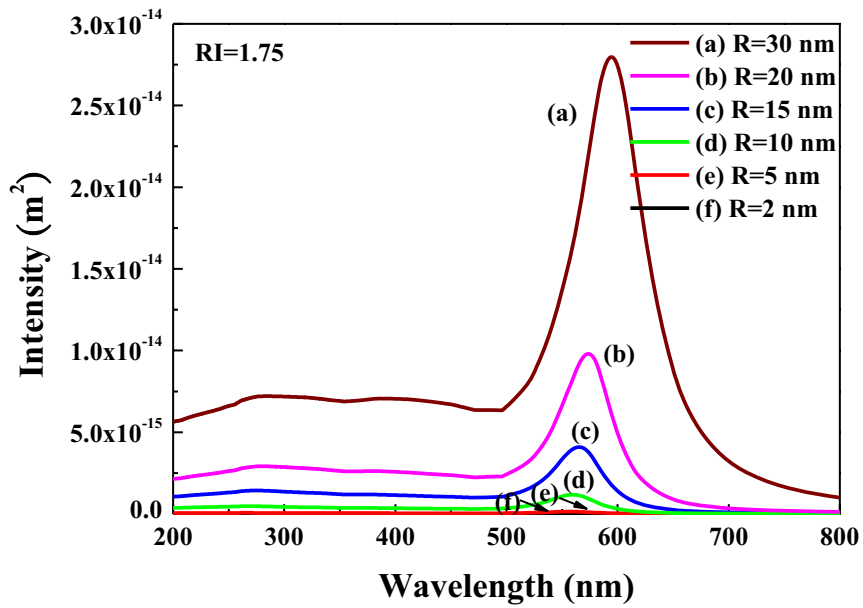
Fig. 4-4. Mieplot simulation of extinction function vs. wavelength when different size of gold spheres were surrounded by RI equaling 1.75.
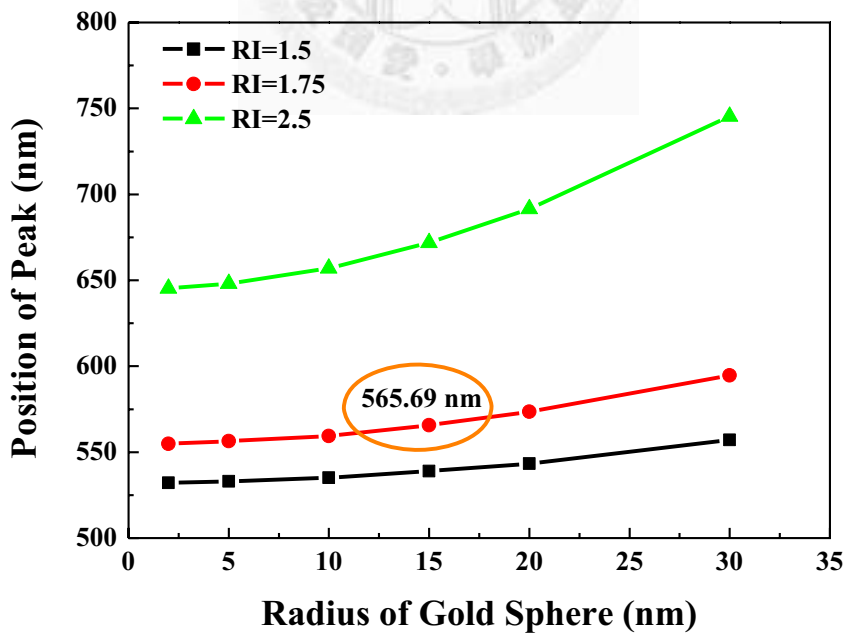
Fig. 4-5. The relationship between the position of LSPR peak and the particle size of gold sphere.

4-2 Photocatalytic Oxidation of Phenol

Although many researchers have tried to investigate the details of photocatalytic oxidation of phenol, the application of Au/TiO_2 in this reaction is not often discussed in literature.

4-2-1 Adsorption of Phenol in Dark Surrounding

The amount of adsorbed phenol on P25 in dark surrounding may be negligible as we demonstrate in Fig. 4-6. The catalyst used was 0.08 g P25, and the 200 mL 250 ppm phenol solution was agitated for 8 hours in dark surrounding. The concentration of phenol remained almost the same as its initial concentration after 8 hours; also, there was no mono-hydroxylated intermediates detected. The affinity of phenol on P25 seems to be quite weak, even though some authors have suggested stirring the solution for about 2 hours or longer before turning the light tubes on, agitating the solution for 10 minutes before turning the light tubes on might be long enough for our system.
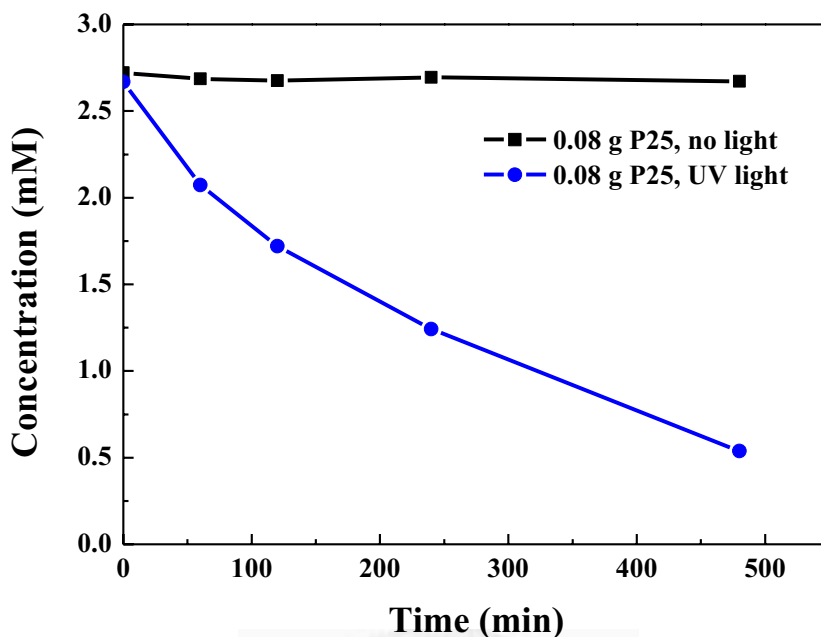
Fig. 4-6. Concentration profiles of phenol in dark surrounding and under the illumination of UV light.

4-2-2 Effect of P25 (TiO$_2$) Powder Content in Solution

The amount of catalyst that should be added into the solution to bring out faster reaction rate varies from case to case, because it has a lot to do with many variables, such as the shape of reactors, the type of catalysts, the characteristic of model compounds, etc. To find out the proper amount of catalyst to be added, the initial concentration of phenol and light source were set to be the same, which meant 250 ppm and 8 300 nm UV light tubes. The concentration of phenol is fitted by first-order kinetics after reaction for 8 hours, and the experimental results are shown in Fig. 4-8.

It can be observed that adding 0.4 g/L catalyst seems to be a better choice

for our system. Even though the rate constant does not show much difference when adding little more or less than 0.4 g/L, this value falls within the suggested amount mentioned in literature [6, 39]. Beyond this value, too much power in the solution may cause a shielding effect on the light, and some active sites on the surface might not be activated; on the other hand, too less powder in the solution may not utilize the light efficiently. Even when there is no catalyst in the solution, the direct photolysis will degrade phenol for about 40 ppm after 8 hours. But with the aid of catalyst, the degraded amount of phenol increases obviously.
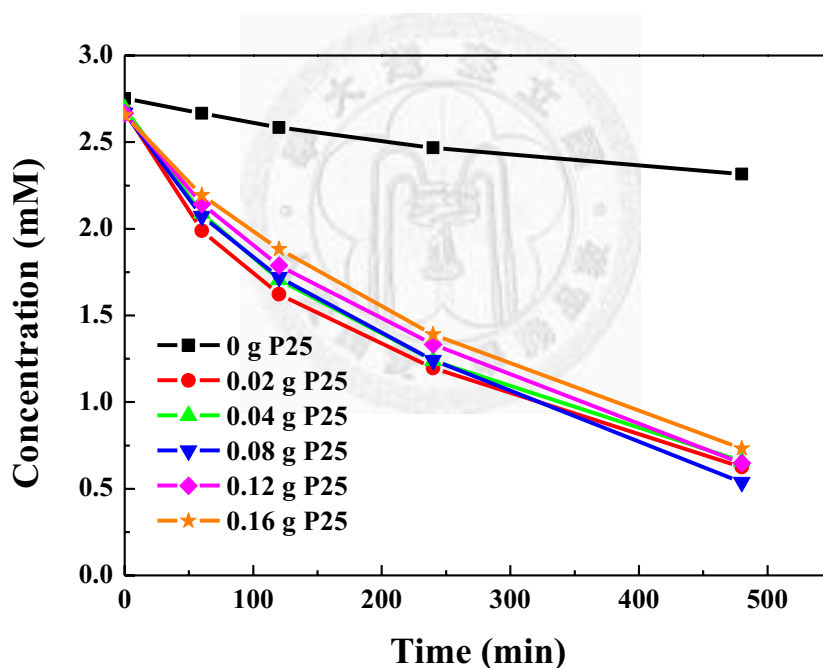

Fig. 4-7. Concentration profiles of phenol when using different amount of P25 as the catalyst, under the irradiation of UV light.
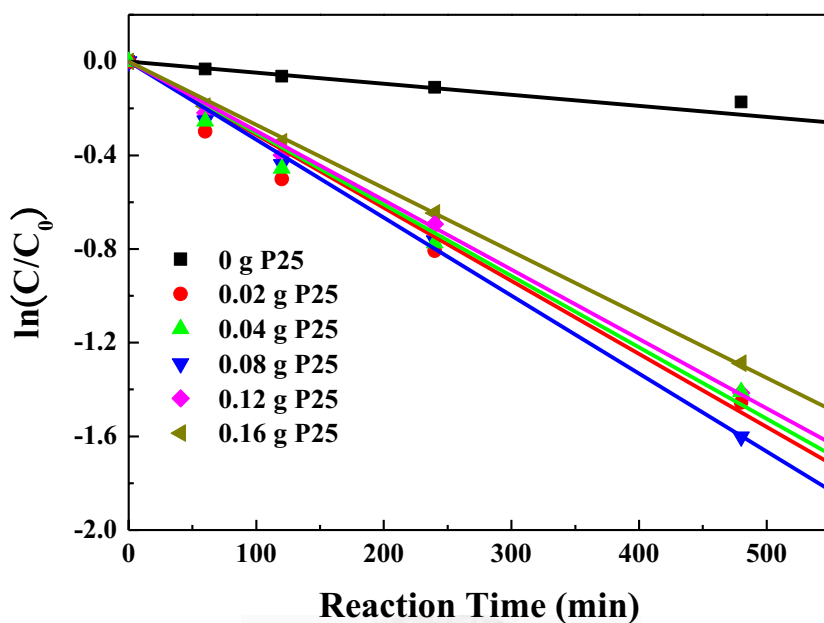
Fig. 4-8. First-order kinetics fitting of the concentration of phenol, under the irradiation of UV light.
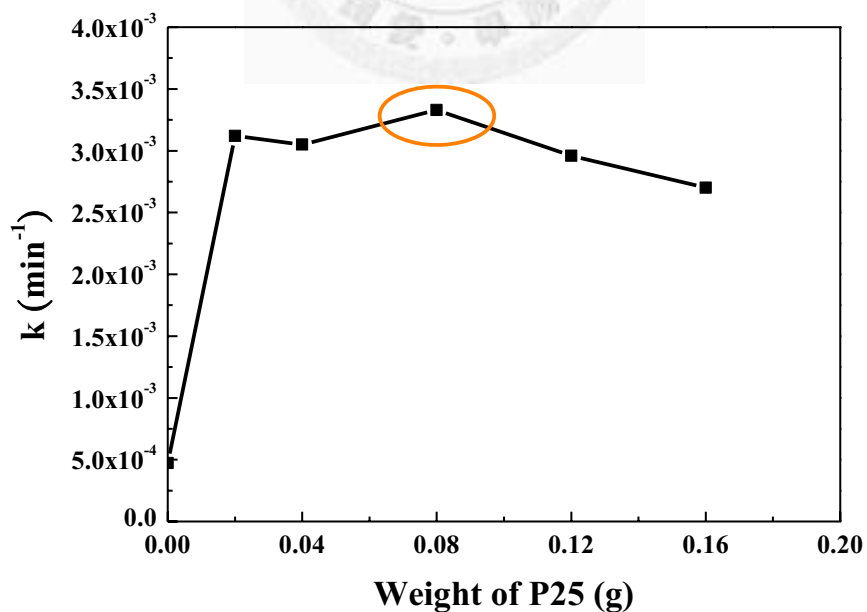
Fig. 4-9. Effect of the amount of P25 in the solution on the reaction rate constant of phenol.

4-2-3 Effect of Initial Concentration and the Amount of Gold on P25

However, the amount of loaded gold seems to have nothing to do with the photocatalytic activity. We think that this does not mean loading more gold on P25 will not contribute to promoting the reaction rate, but because when we want to load more gold on P25, $HAuCl_{4(aq)}$ becomes more acidic, which will destroy the surface of P25 further. The smoothness of the surface of P25 has a lot to do with its photocatalytic activity, too. The original concentration profiles of phenol are shown in Fig. 4-10.

Also, Fig. 4-11 shows that the rate constant is not affected by the initial concentration too much, but is only a characteristic of the catalyst and temperature.
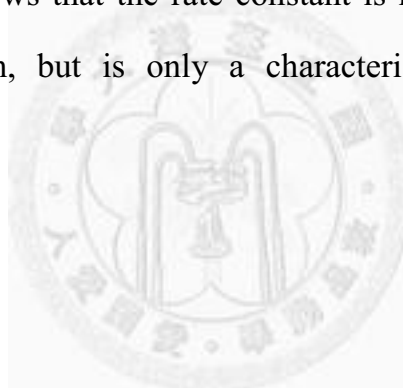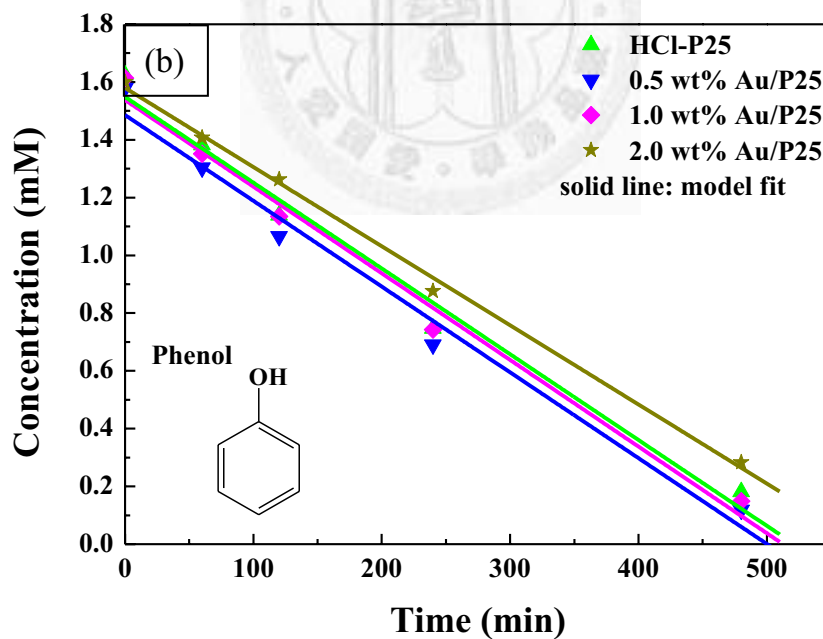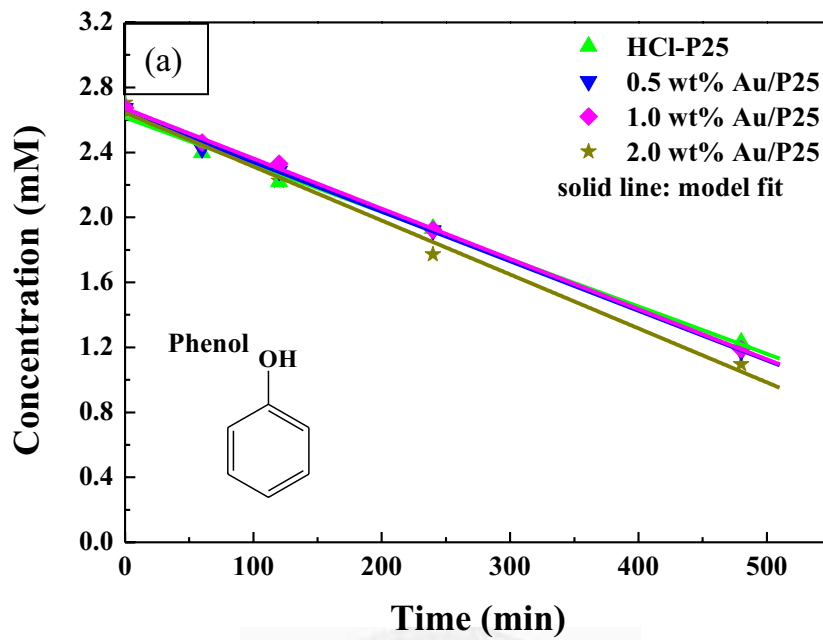
Fig. 4-10. Concentration profiles of phenol at two different initial concentrations, (a) 250 ppm and (b) 150 ppm, under the irradiation of UV light.
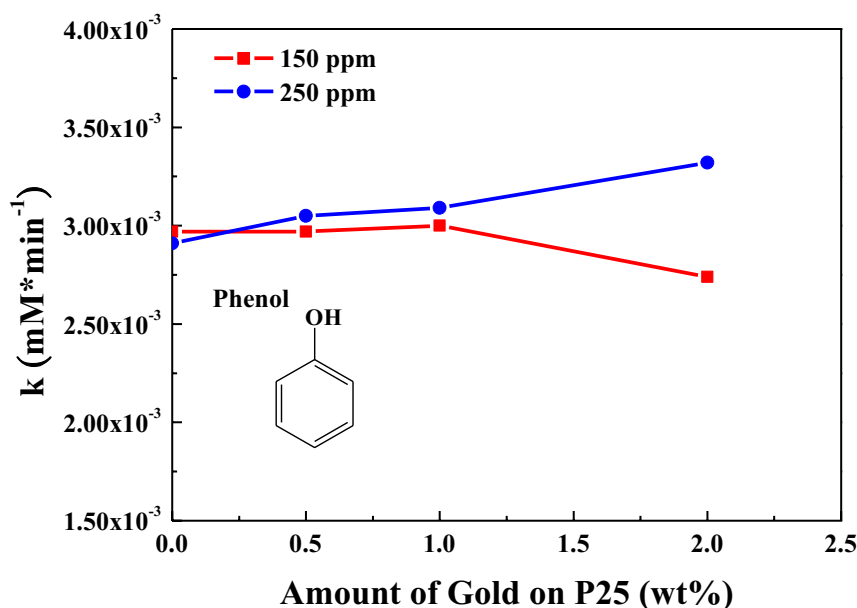
Fig. 4-11. The relationship between the reaction rate constant of phenol and the amount of loaded gold on P25 at two different initial concentrations.

4-2-4 Effect of Temperature

To compare the temperature effect on photocatalytic oxidation of phenol, we selected 4 different temperatures (32℃, 38℃, 45℃, and 55℃) to check the concentration profiles of phenol and its mono-hydroxylated derivatives. The purpose of setting the temperature at 38℃ is that, when visible light tubes and UV light tubes are turned on simultaneously for 60 minutes, the reaction temperature will remain around 38℃. But if only UV light is turned on, the reaction temperature will be raised from room temperature to about 32℃, as is shown in Fig. 4-12. Because starting with lower initial concentration will accelerate the reaction rate, the initial concentration was chosen to be 150 ppm. For pure P25, the degradation rate of phenol drops when the temperature increases from 32℃ to 38℃. For 2.0 wt% Au/P25, the same thing happens

again, but the drop is less obvious than that of P25. Maybe the reason lies in the formation of hydroxyl radicals is not favored when the temperature is elevated, since that the adsorption of water on P25 is an exothermic reaction. Further increasing the temperature would slightly promote the reaction rate for both catalysts. It is hard to calculate the activation energy when using P25 or 2.0 wt% Au/P25 as the catalyst from Fig. 4-16, since that the Arrhenius plot is almost horizontal. The small activation energy of photocatalytic oxidation of phenol also confirms with what we have mentioned in Chap. 2-2-2 for other photocatalytic reactions.

Although the concentration of phenol does not vary much when changing the temperature, the concentration profiles of mono-hydroxylated intermediates show that temperature do have some influences on the reaction. From Fig. 4-14 and Fig. 4-15, the trend of the concentration profiles of 1,4-benzenediol and 1,2-benzenediol all climbs to a maximum value and then goes down. Because the quantity of hydroxyl radicals in the solution increases as the reaction proceeds, initially only phenol is degraded, but the intermediates will also be mineralized if the reaction time is long enough. The formation amount of mono-hydroxylated intermediates is related to their chemical structures. For 1,3-benzenediol, since that it is not favored to be attacked by hydroxyl radicals, the formation amount is relative fewer than 1,2-benzenediol and 1,4-benzenediol. When being illuminated for the same time, the concentration of 1,2-benzenediol is often higher than 1,4-benzenediol, one of the reasons may be because 1,4-benzenediol forms intermolecular hydrogen bond among each other, which will create like a shield against the attack of hydroxyl radicals, whereas 1,2-benzenediol largely forms intramolecular hydrogen bond, as is

shown in Fig. 4-17. Therefore, 1,2-benzenediol is more vulnerable to be further oxidized. The reason of operating the experiment more time when using 2.0 wt% Au/P25 is that, because P25 reacts faster than 2.0 wt% Au/P25, four hours is long enough for us to see the change in reaction kinetics.
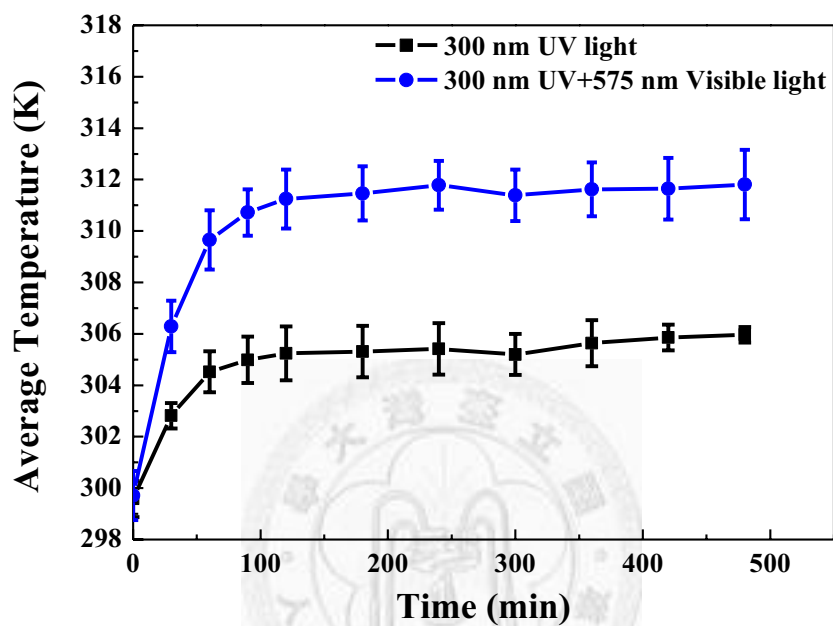
Fig. 4-12. Temperature profiles of phenol solution as the reaction proceeds.
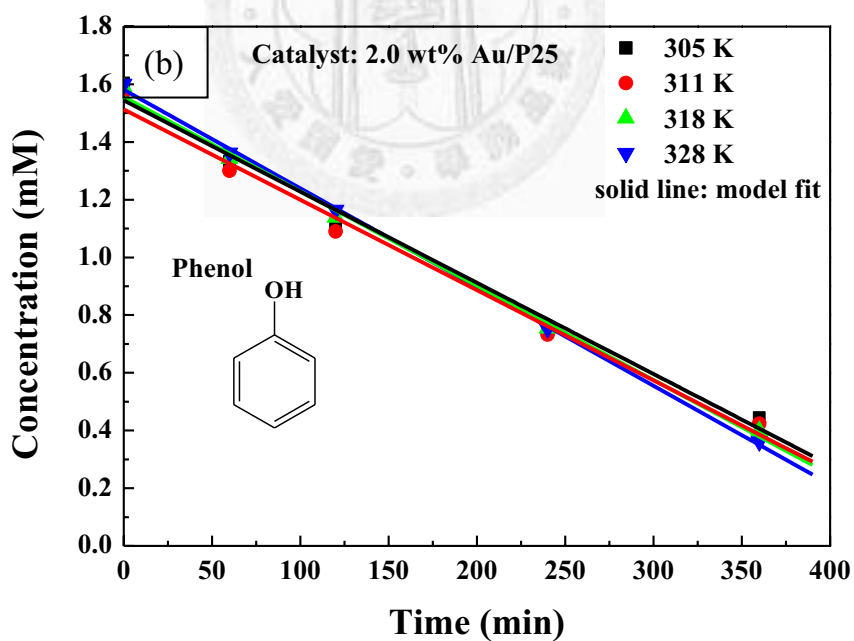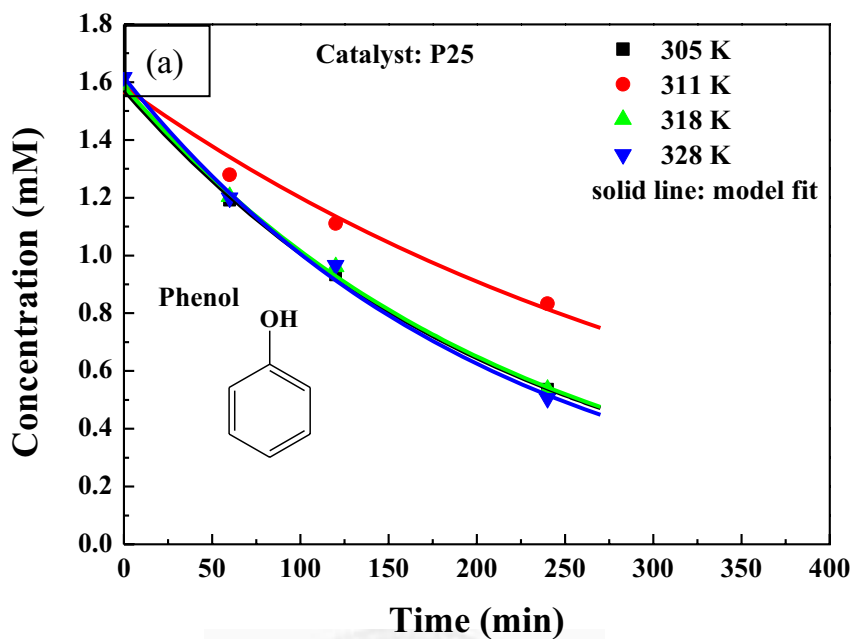
Fig. 4-13. Concentration profiles of phenol at different temperatures when using (a) P25 and (b) 2.0 wt% Au/P25 as the catalyst.
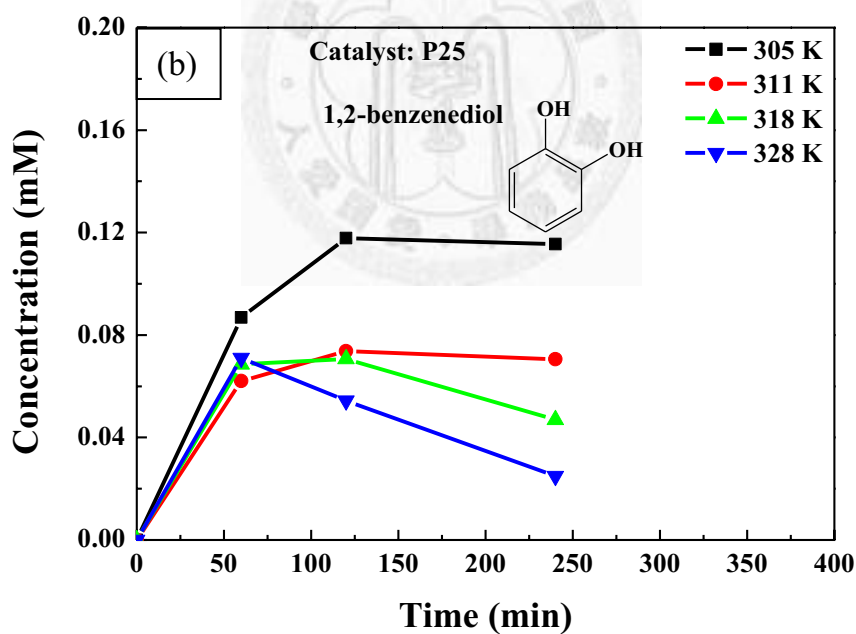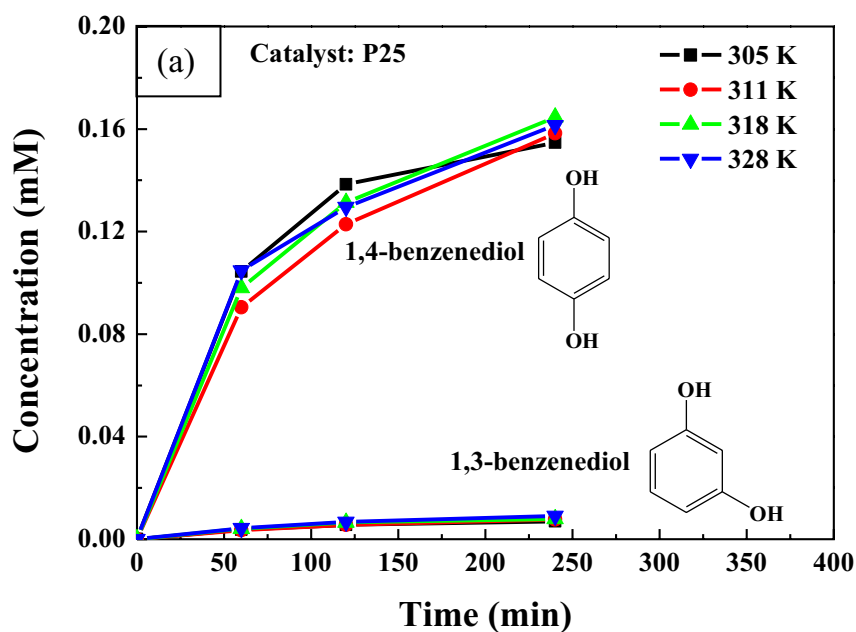
Fig. 4-14. Mono-hydroxylated intermediates distribution when using P25 as the catalyst. (a) 1,4-benzenediol and 1,3-benzenediol, (b) 1,2-benzenediol.
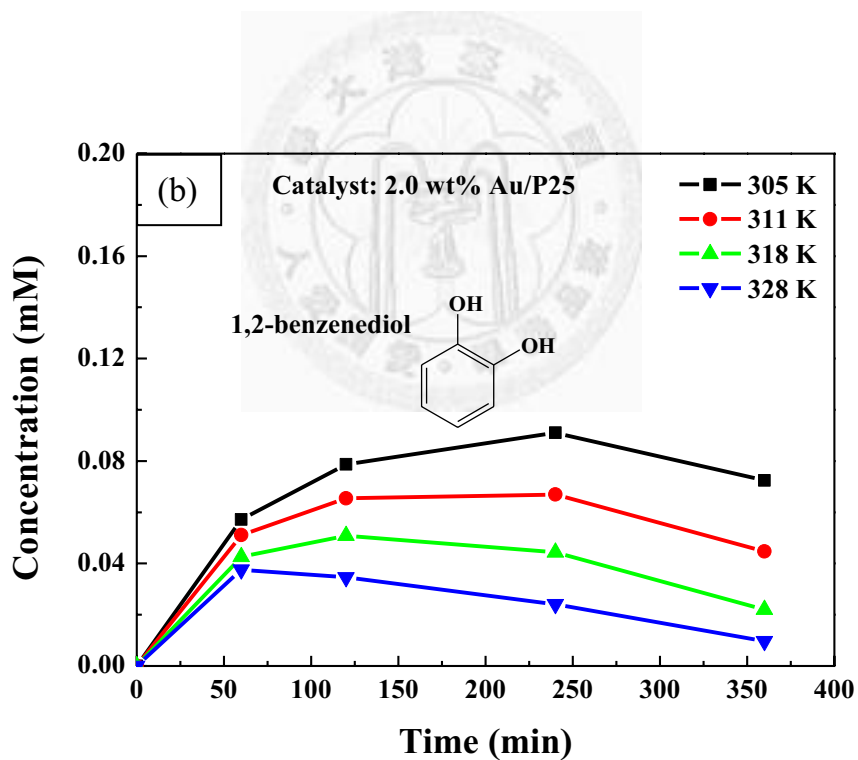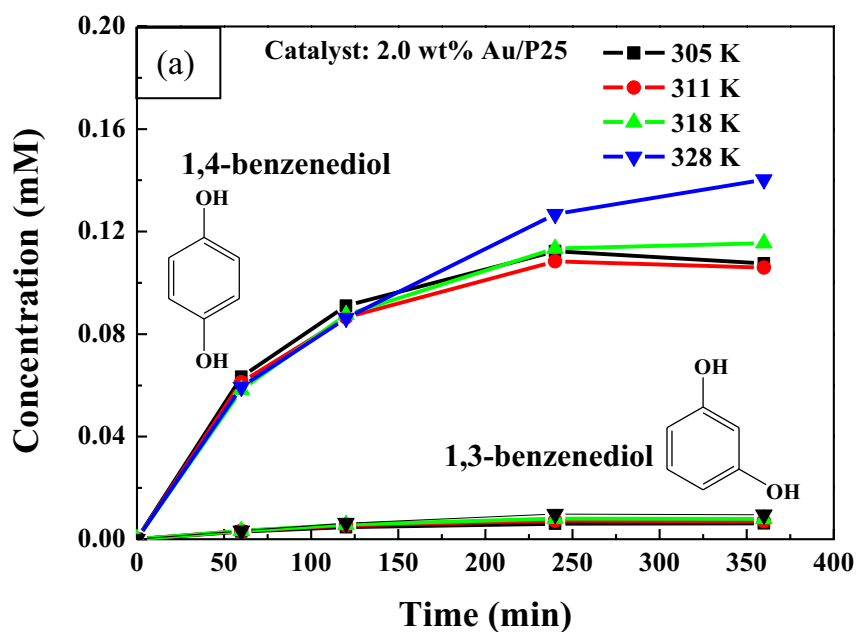
Fig. 4-15. Mono-hydroxylated intermediates distribution when using 2.0 wt% Au/P25 as the catalyst. (a) 1,4-benzenediol and 1,3-benzenediol, (b) 1,2-benzenediol.
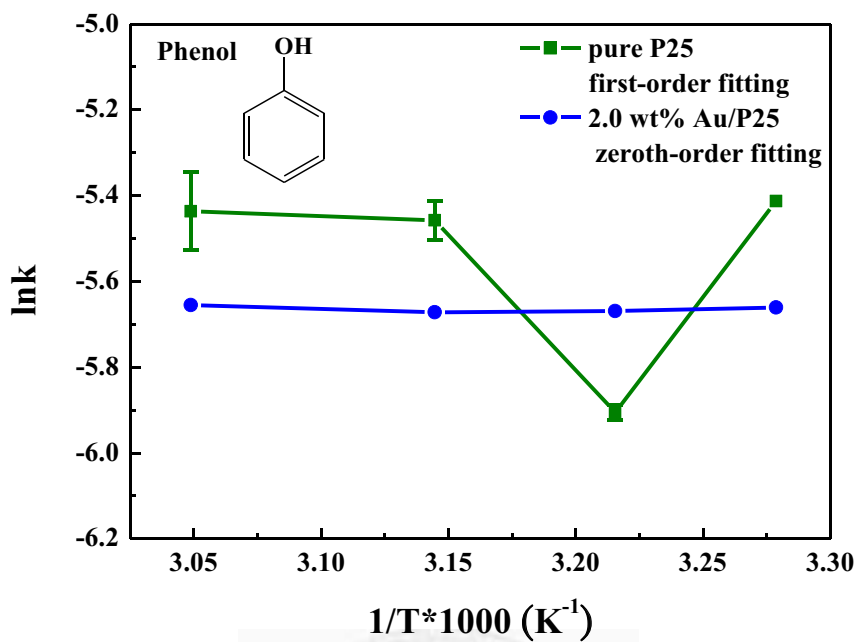
Fig. 4-16. The reaction rate constant of phenol at different temperatures.
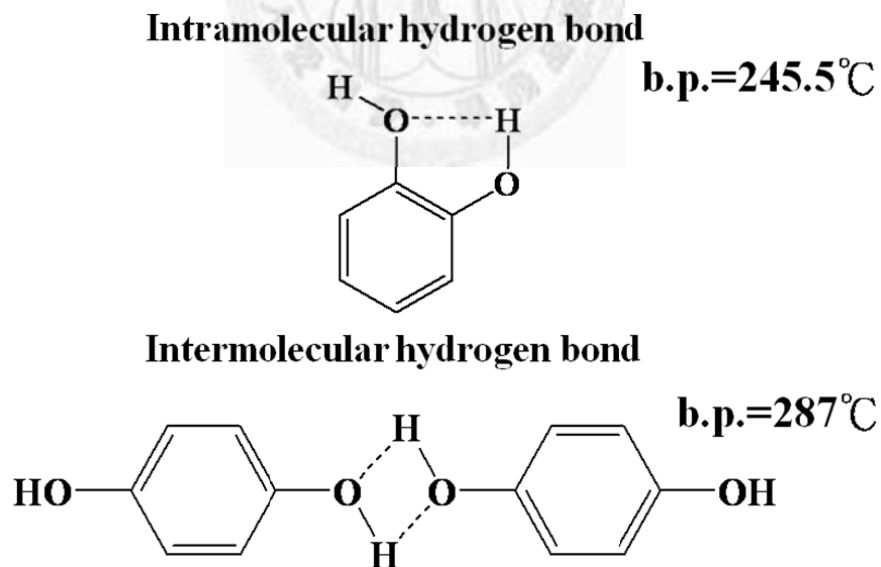
Fig. 4-17. The intramolecular hydrogen bond and intermolecular hydrogen bond of 1,2-benzenediol and 1,4-benzenediol, respectively.

4-2-5 Possible Mechanism

Besides knowing the kinetics model of phenol itself, we also want to investigate the concentration profiles of the main mono-hydroxylated intermediates; namely, 1,2-benzenediol and 1,4-benzenediol. Eq. (4-1)~(4-3) are deduced from [40], and we want to know whether this model can be applied to our system. The detailed parts of the fitting steps are illustrated in Appendix A.

$$\frac{dC_1}{dt} = -kC_1 \text{ or } -k \tag{4-1}$$

$$\frac{dC_2}{dt} = k_1 C_1 - k_3 C_2 \tag{4-2}$$

$$\frac{dC_3}{dt} = k_2 C_1 - k_4 C_3 \tag{4-3}$$
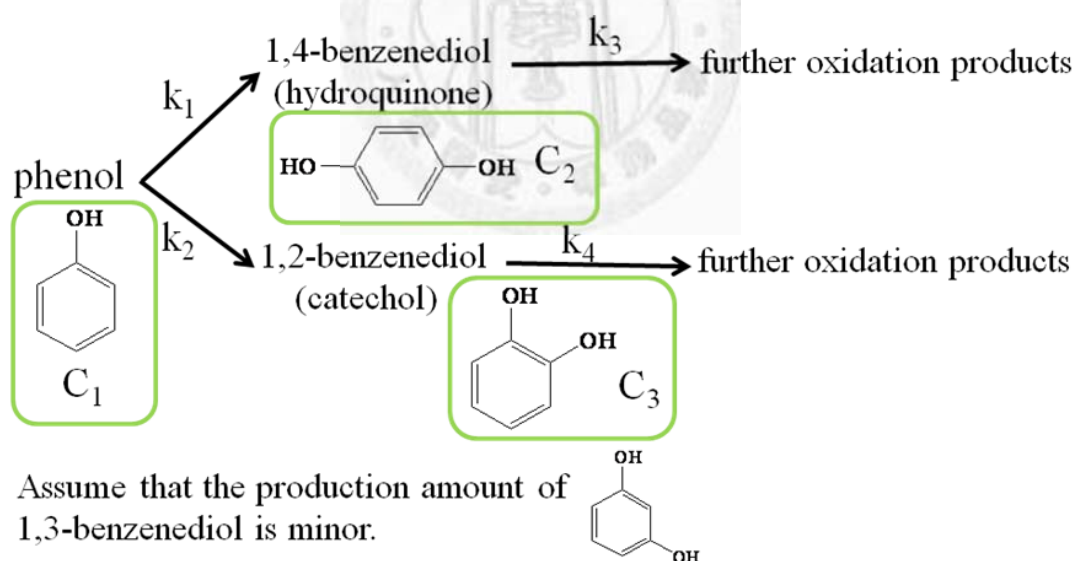
Fig. 4-18. Schematic drawing of the proposed mechanism [40].

4-2-6 Model Fitting-Initial Concentration Effect

Fig. 4-19 can be viewed as the mass balance of carbon in the solution, because phenol is the only carbon source. According to the mechanism mentioned in Chap. 4-2-5, the decrease in the concentration of phenol should be converted to the mono-hydroxylated intermediates first. The sum of the concentration of the three mono-hydroxylated intermediates is equal to the concentration of the benzene rings, and so is the concentration of phenol. The decrease in the concentration of phenol is greater than the increase in the concentration of the sum of mono-hydroxylated intermediates, which means that the amount of carbon is not balanced, and may imply that the degradation pathway of phenol is not only via the attack of hydroxyl radicals, but may be through the adsorption of phenol on the catalyst and then be mineralized directly. Because theoretically, k_1+k_2 should be equal to k in order to satisfy the law of mass conservation, but the calculated results show that k_1+k_2 is about one-third of k.
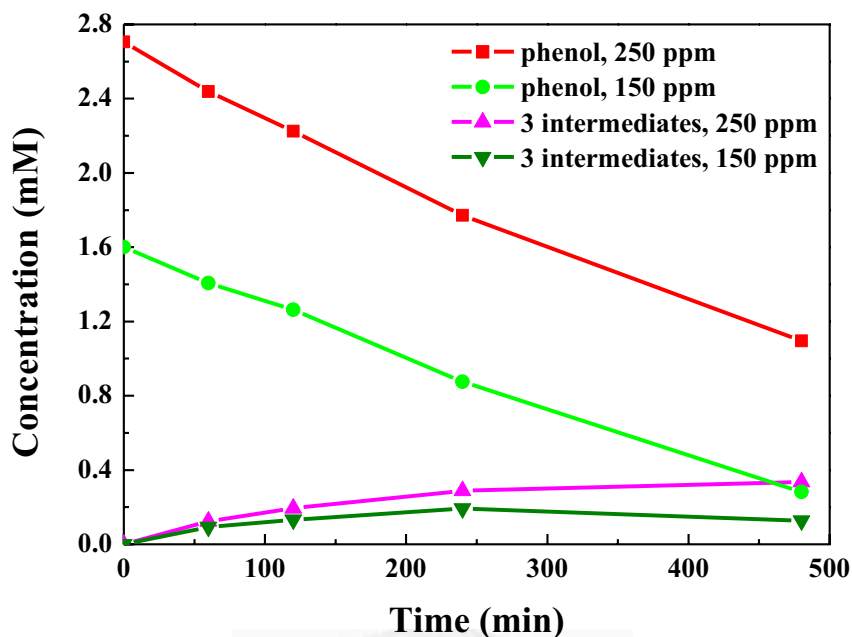
Fig. 4-19. The concentration profiles of phenol and the sum of the three mono-hydroxylated intermediates at two different initial concentrations. The catalyst used is 2.0 wt% Au/P25, and the light source is UV light only.

Fig. 4-20 and Fig. 4-21 show the kinetics model fitting result of 1,2-benzenediol and 1,4-benzenediol, we can find that the difference between the formation rate constants (k_1 and k_2) is smaller when the amount of gold on P25 increases, which may imply that the selectivity is also getting closer.

The selectivity of 1,2-bezenediol and 1,4-benzenediol is defined as follows:

$$1,2\text{-benzenediol (mol\%)} = \frac{1,2\text{-benzenediol}}{1,2\text{-benzenediol} + 1,3\text{-benzenediol} + 1,4\text{-benzenediol}} \quad (4\text{-}4)$$

$$1,4\text{-benzenediol (mol\%)} = \frac{1,4\text{-benzenediol}}{1,2\text{-benzenediol} + 1,3\text{-benzenediol} + 1,4\text{-benzenediol}} \quad (4\text{-}5)$$

Fig. 4-22 demonstrates the selectivity of 1,2-benzenediol and 1,4-benzenediol as the reaction proceeds. When using 2.0 wt% Au/P25 as the catalyst, the selectivity of 1,2-benzenediol and 1,4-benzenediol is quite close before 240 minutes, and that is why we want to further compare the temperature effect when applying P25 and 2.0 wt% Au/P25 as the catalyst, respectively.
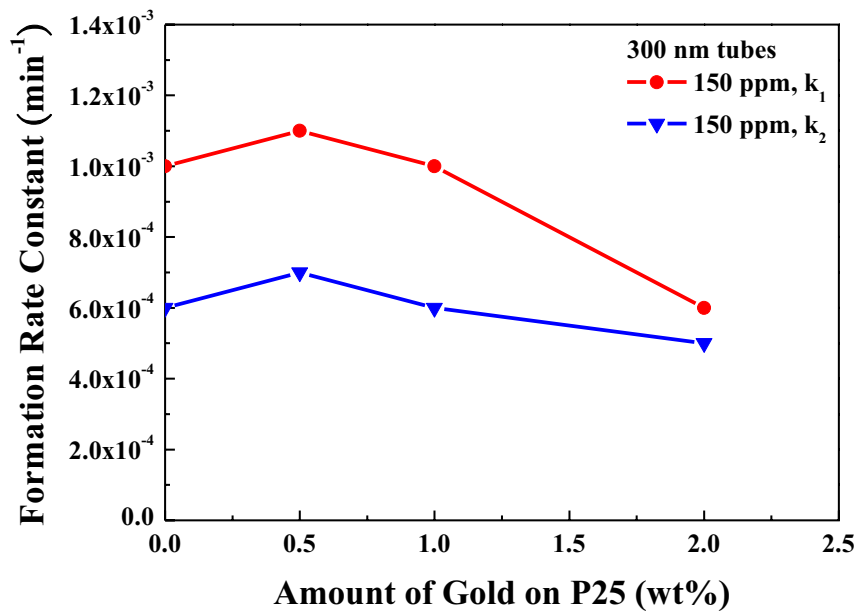
Fig. 4-20. The relationship between the formation rate constants and the amount of gold on P25.
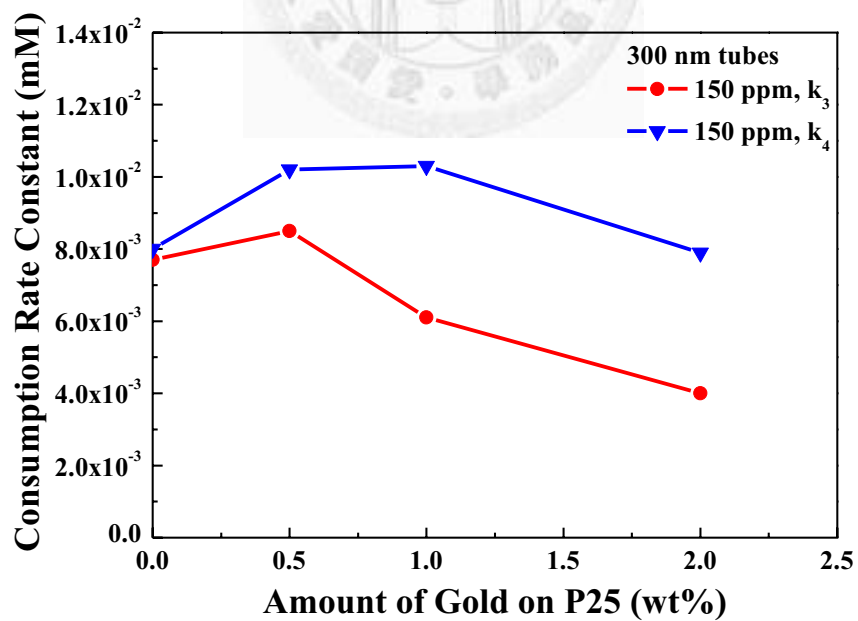
Fig. 4-21. The relationship between consumption rate constants and the amount of gold on P25.
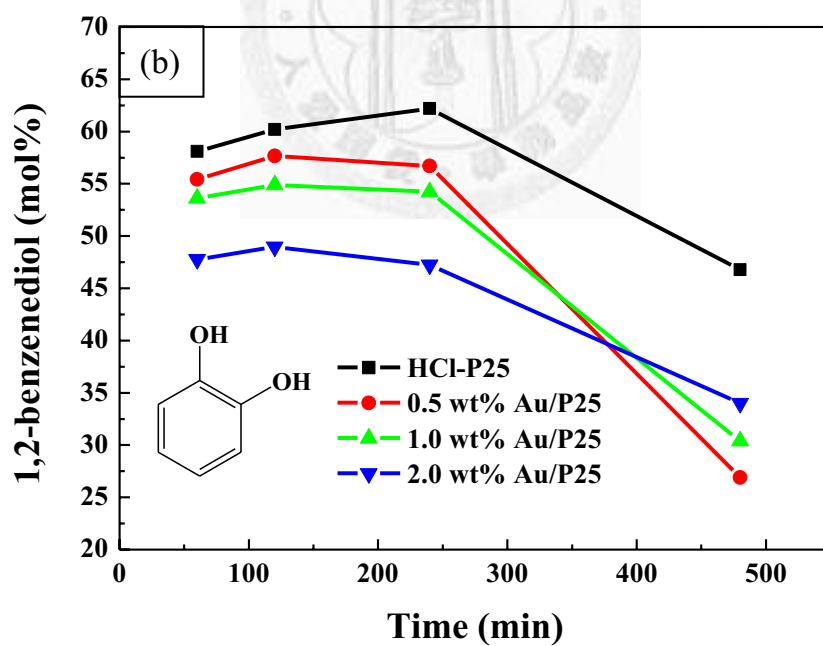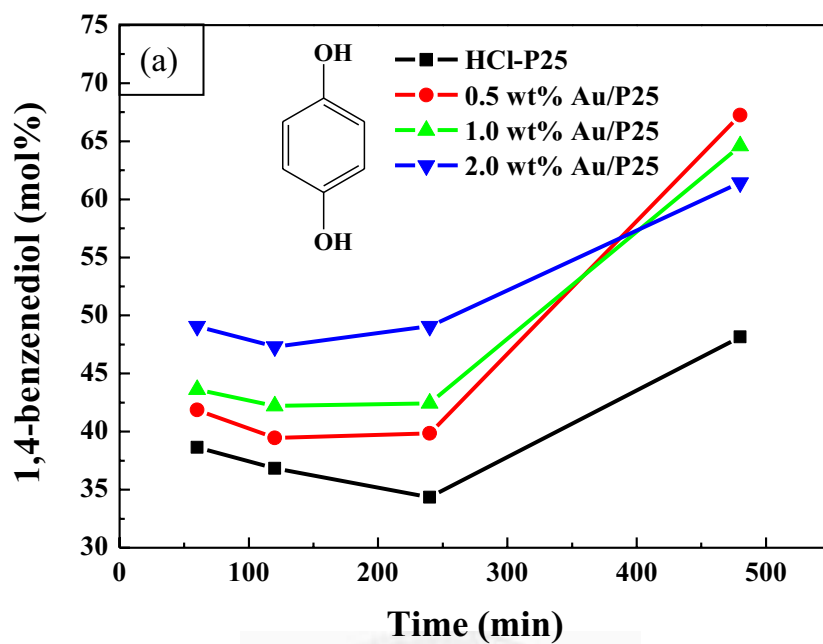
Fig. 4-22. Selectivity of (a) 1,4-benzenediol and (b) 1,2-benzenediol when the initial concentration of phenol is 150 ppm.

4-2-7 Model Fitting-Temperature Effect

Fig. 4-23 and Fig. 4-24 are the concentration profiles of 1,2-benzenediol and 1,4-benzenediol when using P25 and 2.0 wt% Au/P25 as the catalyst, respectively. The data points are measured with LC-UV, and the solid lines are the solutions of C_2 and C_3 of Eq. (4-2) and Eq. (4-3). In addition, Fig. 4-25 is the Arrhenius plot of 1,2-benzenediol and 1,4-benzenediol, just as the Arrhenius plot of phenol in Fig. 4-16, the mono-hydroxylated intermediates might not be affected by temperature very much, because their activation energy cannot be obtained from the Arrhenius plot, either.

Fig. 4-26 and Fig. 4-27 illustrate the selectivity of 1,4-benzenediol and 1,2-benzenediol, even though the concentration of phenol in Fig. 4-13 does not vary too much, the selectivity of 1,4-benzenediol is getting higher with the increase of temperature and time, and this phenomenon again demonstrates the benefit of intermolecular hydrogen bond, which is more resistant to the increase in temperature.
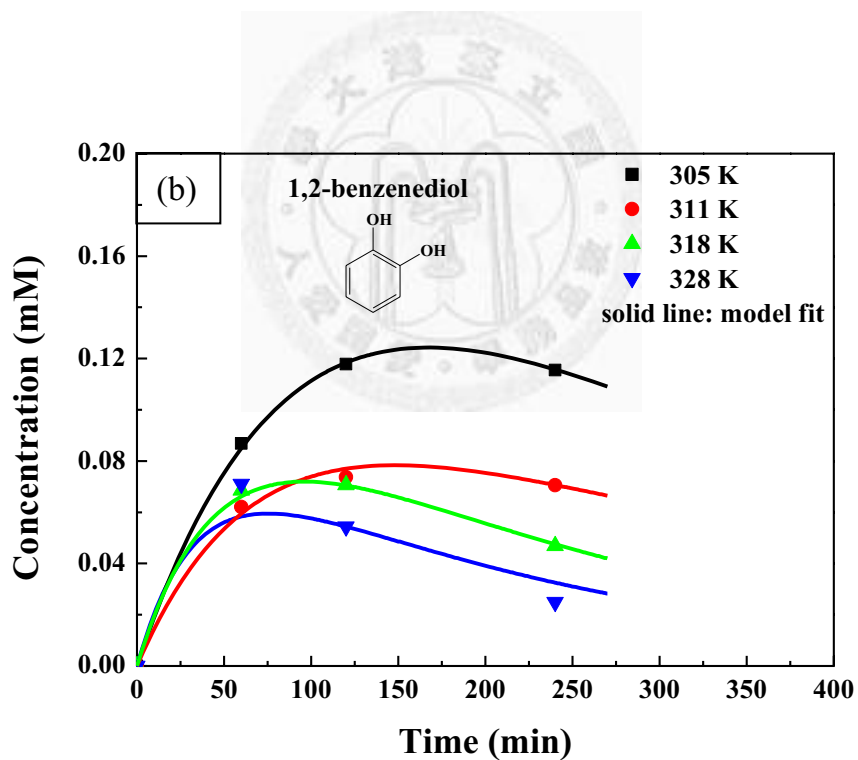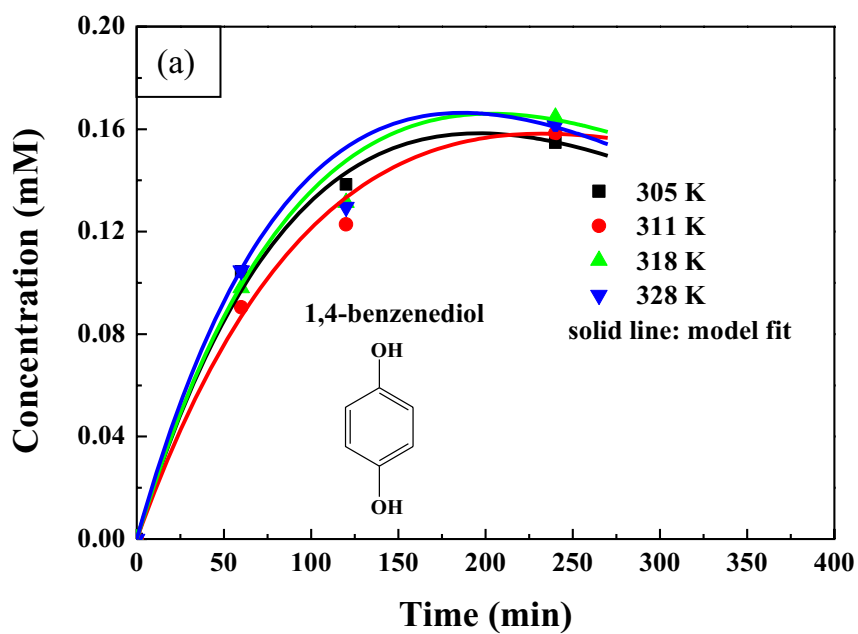
Fig. 4-23. Concentration profiles when using P25 as the catalyst at different temperatures. (a) 1,4-benzenediol and (b) 1,2-benzenediol.
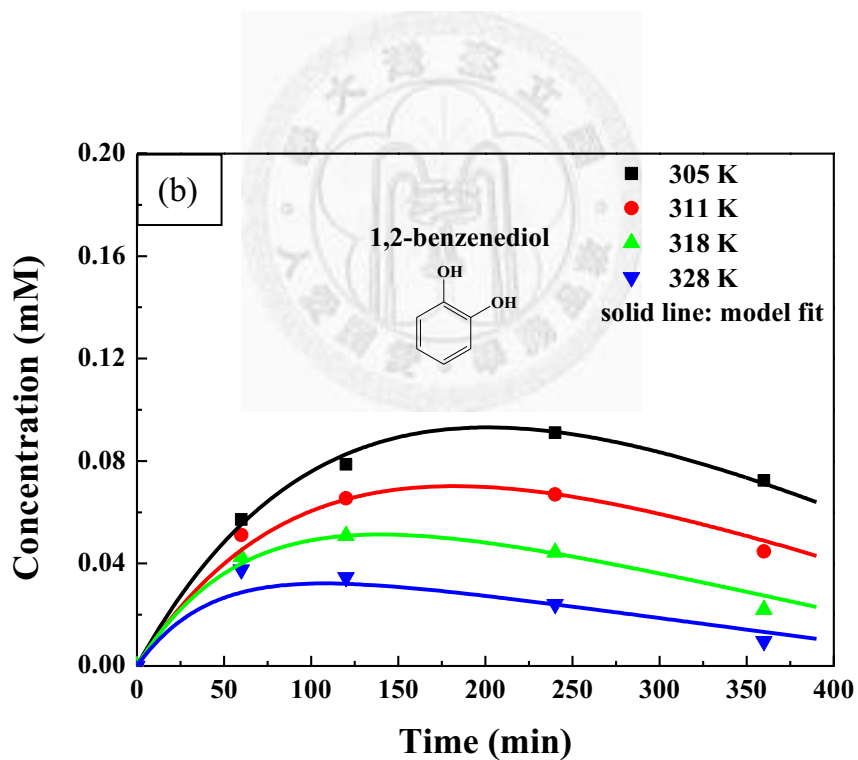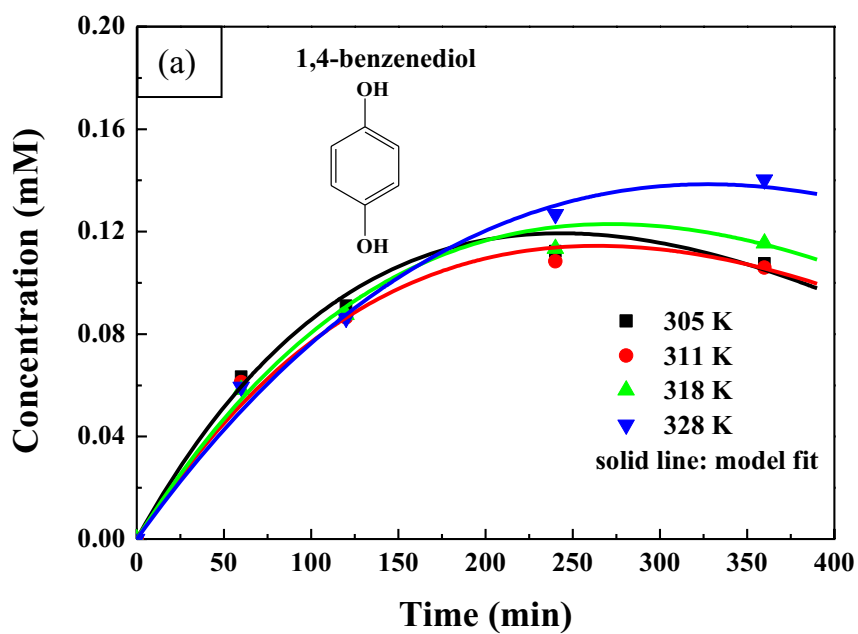
Fig. 4-24. Concentration profiles when using 2.0 wt% Au/P25 as the catalyst at different temperatures. (a) 1,4-benzenediol and (b) 1,2-benzenediol.
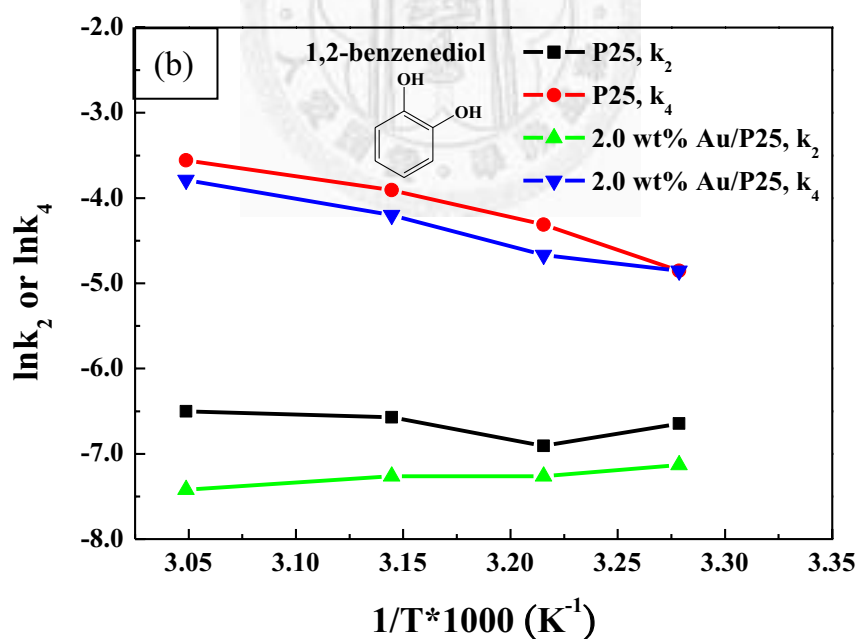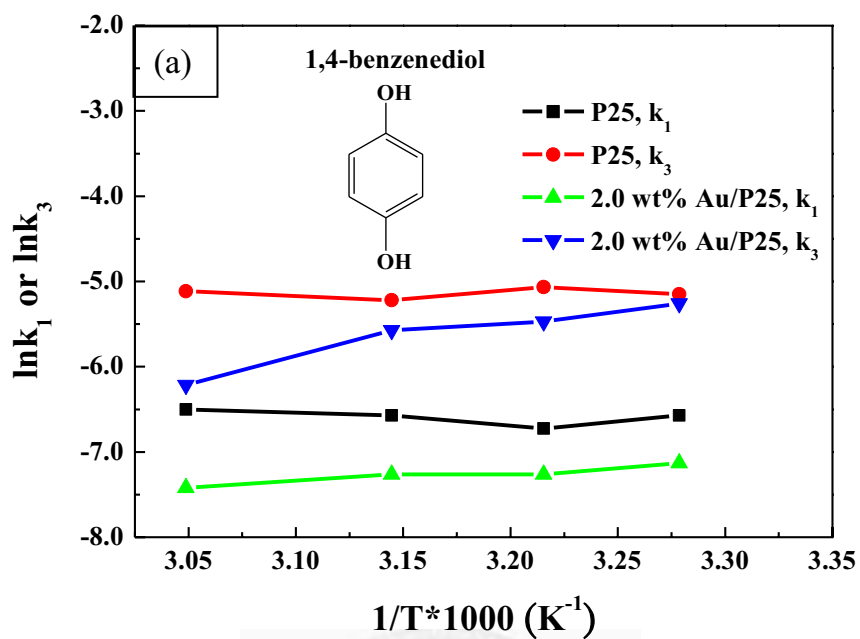
Fig. 4-25. The Arrhenius plot of (a) 1,4-benzenediol and (b) 1,2-benzenediol when using P25 and 2.0 wt% Au/P25 as the catalyst, respectively.
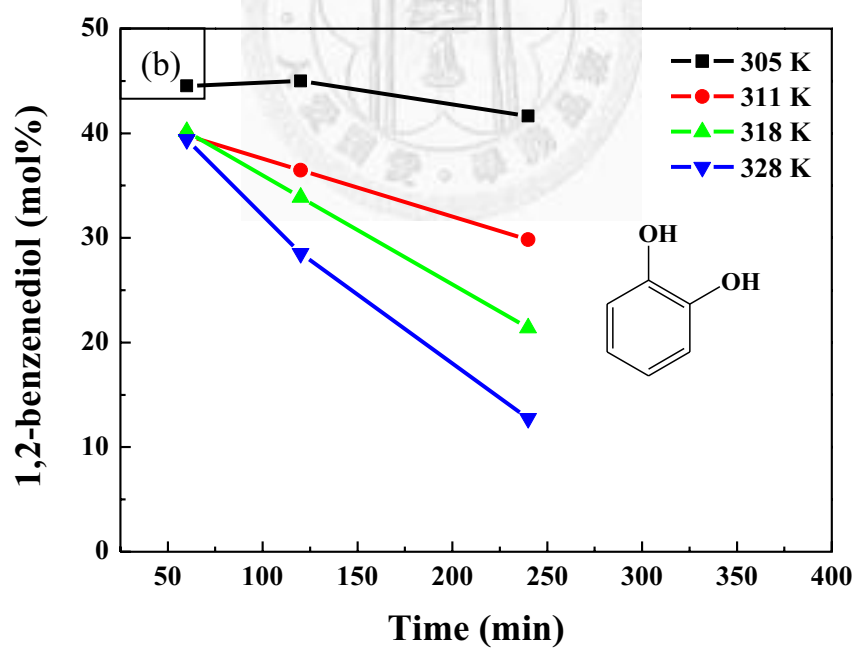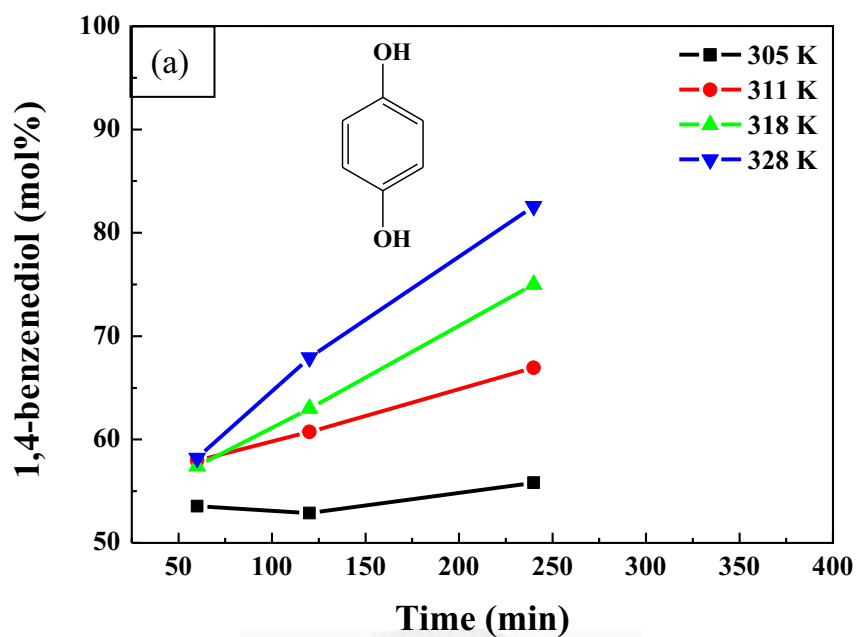
Fig. 4-26. Selectivity of (a) 1,4-benzenediol and (b) 1,2-benzenediol when using P25 as the catalyst.
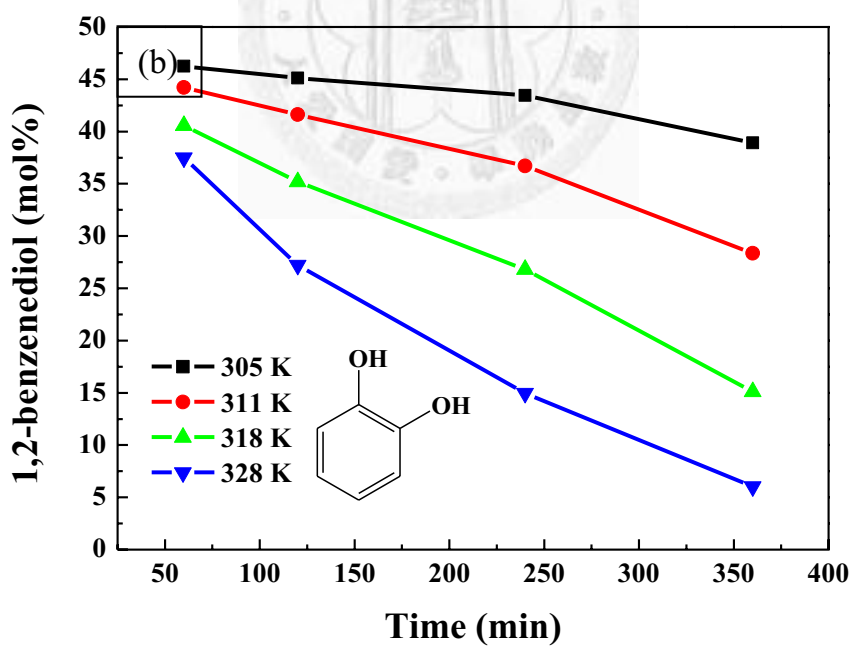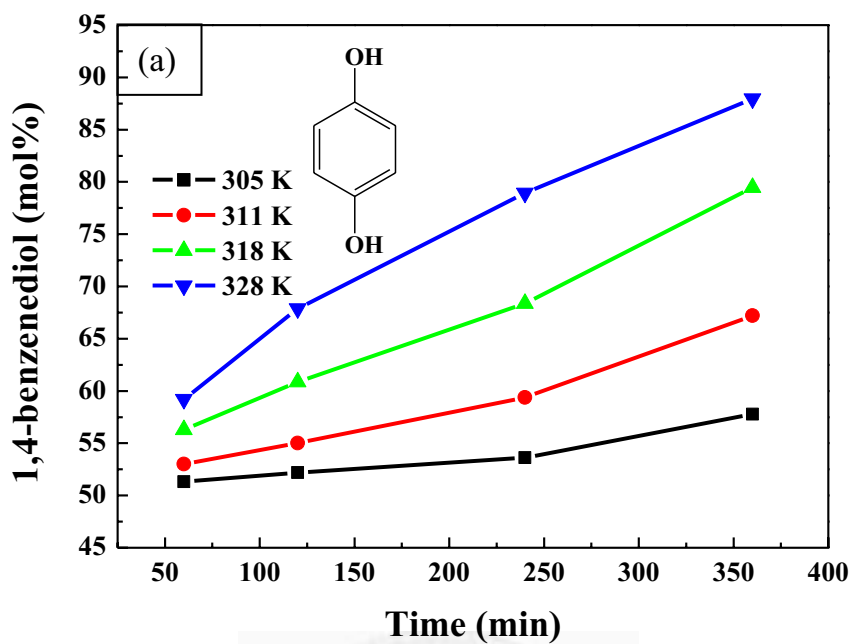
Fig. 4-27. Selectivity of (a) 1,4-benzenediol and (b) 1,2-benzenediol when using 2.0 wt% Au/P25 as the catalyst.

4-2-8 Visible Light Effect

The purpose of illuminating the phenol solution with UV and visible light sources is trying to realize how much LSPR effect can enhance the reaction rate. Fig. 4-29 shows that using dual light sources can elevate the degradation rate of phenol. Although the reaction temperature of phenol solution is different when turning visible light tubes on simultaneously, we did another experiment attempting to prove that the elevation in reaction rate is not because of the temperature effect, but because of the LSPR effect. The experimental result is shown is Table 4-1. When illuminated by UV light only, the rate constant of phenol remains almost the same despite raising the reaction temperature about 6℃.
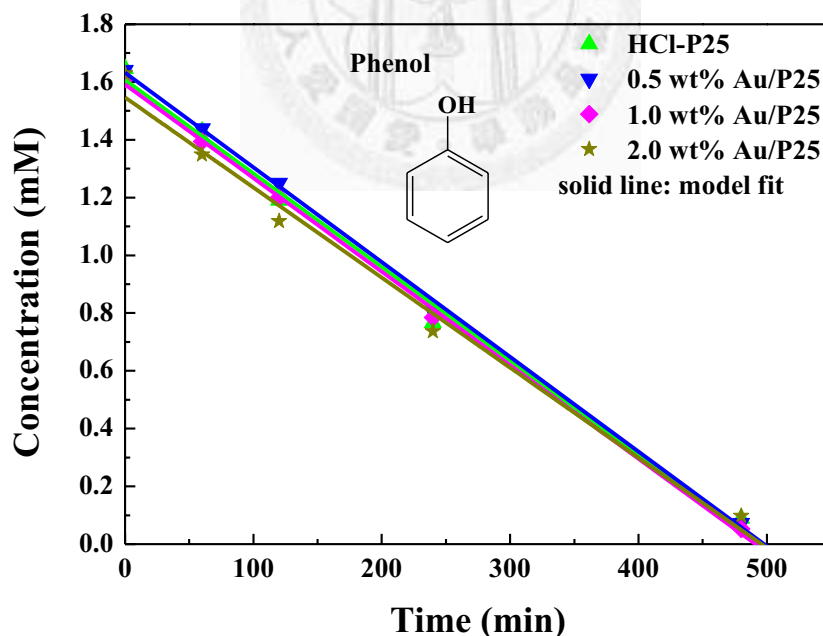
Fig. 4-28. Concentration profiles of phenol under the irradiation of UV and visible light sources.
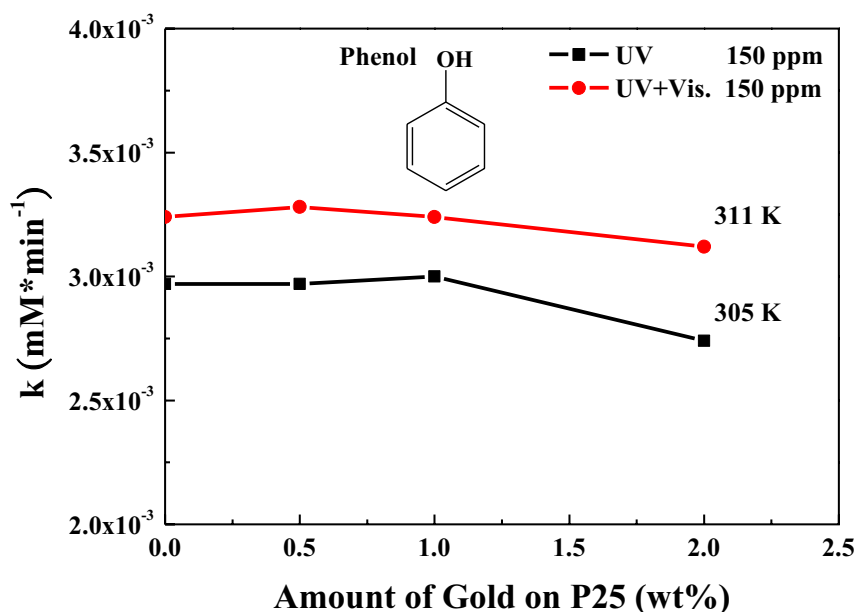
Fig. 4-29. LSPR effect on the enhancement of the degradation rate of phenol.

Table 4-1. Temperature effect on the reaction rate constant of phenol.

	2.0 wt% Au/P25
UV, 305 K	k=3.16E-3 mM*min^{-1}
UV, 311 K	k=3.13E-3 mM*min^{-1}

However, for 1,2-benzenediol and 1,4-benzenediol, the LSPR seems to have no obvious effect on the concentration profiles, as is displayed in Fig. 4-30 and Fig. 4-31. If we look at Fig. 4-32, we can observe that when under the irradiation of UV and visible light, the formation rate constants, k_1 and k_2, increase with the increase of gold on P25. While the consumption rate constants, k_3 and k_4, do not increase apparently or remain nearly constant with the increase of gold on P25; however, k_3 and k_4 decrease as the amount of gold

on P25 increases under the illumination of UV light only, which may imply that LSPR effect promotes the consumption rate constants from another angle.

At low loaded amount of gold on P25, using dual light sources appears to be not advantageous over using UV light only. It does not mean that LSPR do not happen, but because the increase in temperature of about $6℃$ may not be beneficial to the formation of hydroxyl radicals, and thus the production of mono-hydroxylated intermediates is also hindered. But when the loaded amount is high enough, LSPR effect can surpass the temperature effect, so we can observe some enhancement in the rate constants.
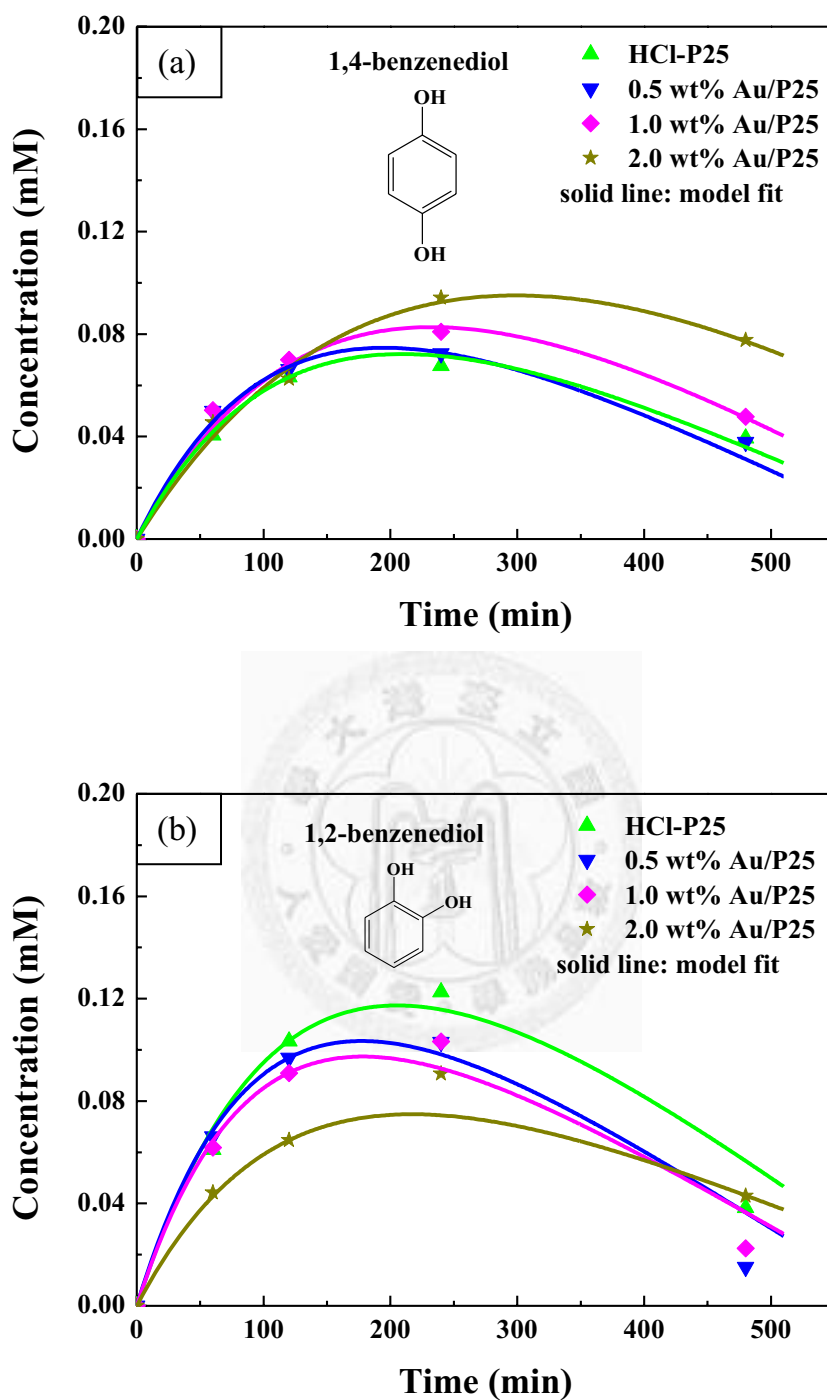
Fig. 4-30. Concentration profiles of the main mono-hydroxylated intermediates, (a) 1,4-benzenediol and (b) 1,2-benzenediol, under the illumination of UV light.
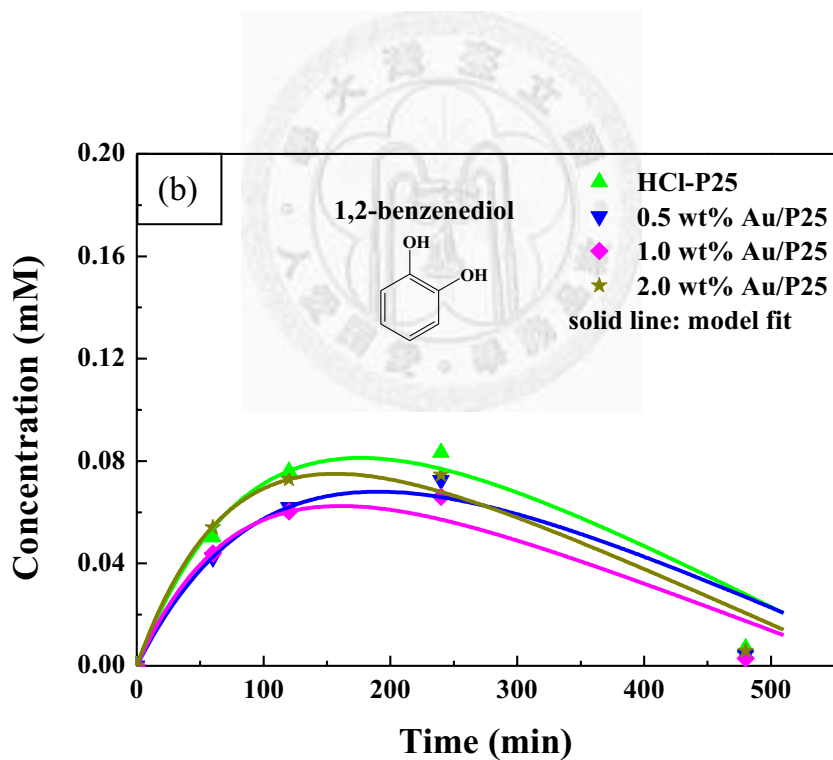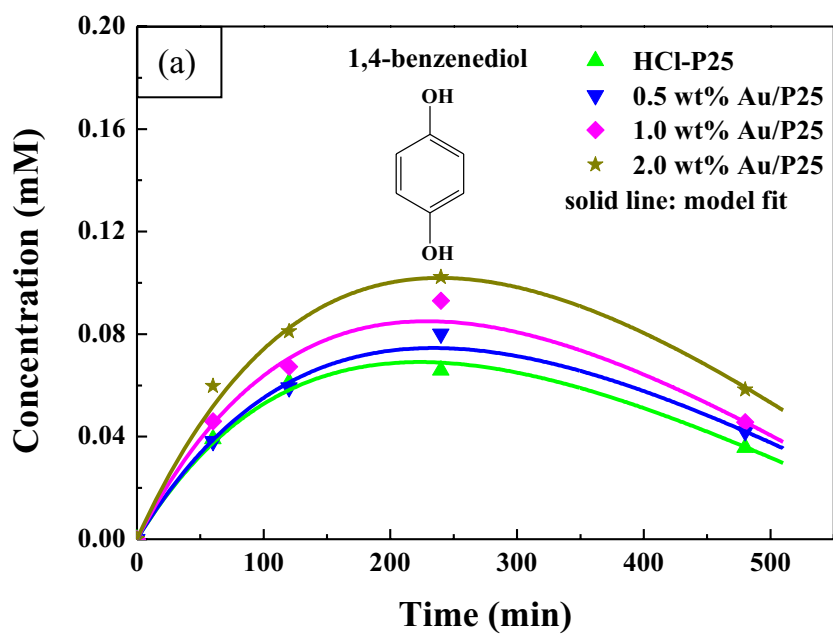
Fig. 4-31. Concentration profiles of the main mono-hydroxylated intermediates,
(a) 1,4-benzenediol and (b) 1,2-benzenediol, under the illumination of UV and
visible light.
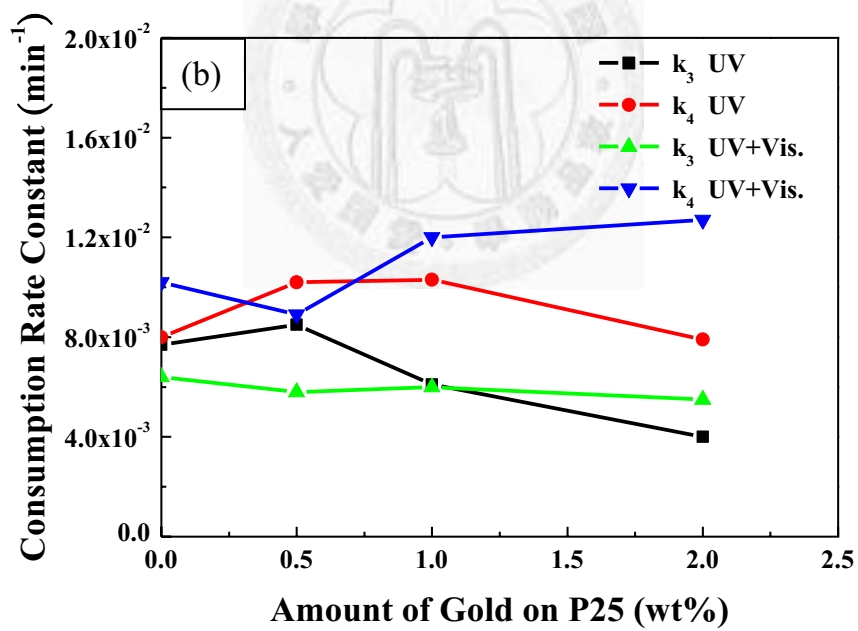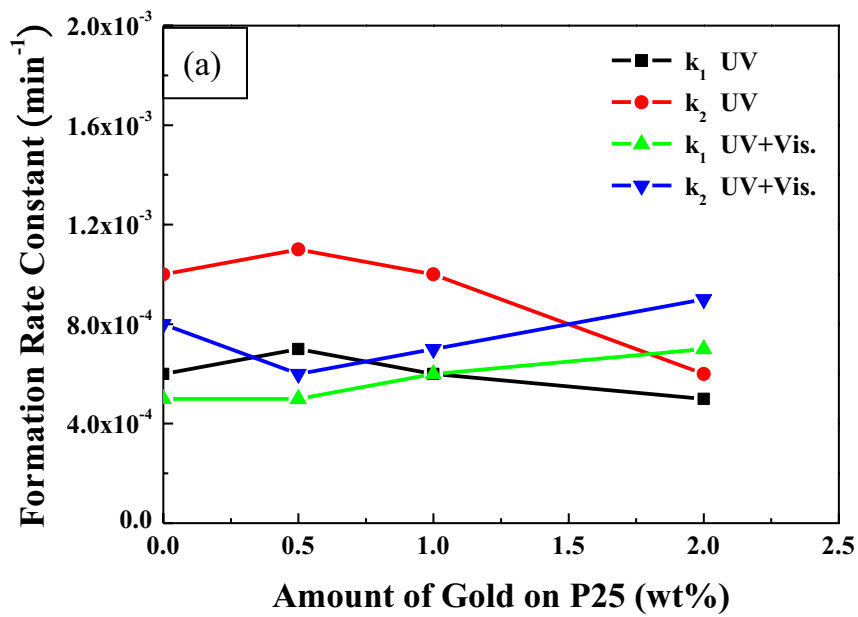
Fig. 4-32. (a) Formation rate constant and (b) consumption rate constant under the irradiation of UV only or UV and visible light.

Chapter 5 Conclusion

Photocatalytic oxidation of phenol solution was investigated in this research. Several parameters, such as initial concentration, temperature, amount of gold on P25, LSPR effect, had their influences on the concentration profiles of phenol or the main mono-hydroxylated intermediates.

When we used P25 as the catalyst, the concentration of phenol followed first-order kinetics model, and its photocatalytic activity was greater than Au/P25 under the same experimental conditions, partly because the surface of Au/P25 was destroyed after treated with acidic $HAuCl_{4(aq)}$. The reaction rate constant of phenol was independent of its initial concentration, and it did not vary obviously with the amount of gold on P25, either.

In regard to the temperature effect, we cannot obtain the activation energy of phenol or the main mono-hydroxylated intermediates in the temperature range of 32~45°C, no matter when we used 2.0 wt% Au/P25 or P25 as the catalyst. Maybe it is because the adsorption and surface reaction steps are in competition with the rate-determining step within this temperature range.

In addition, the simplified mechanism can approximately describe the concentration profiles of phenol and the main mono-hydroxylated intermediates obtained from LC-UV. Although k_1+k_2 is not equal to k, these data remind us that there exist other possible reaction mechanisms occurring at the same time.

Finally, we observe some enhancement in the degradation rate of phenol owing to LSPR effect. While the rate constants of the main mono-hydroxylated intermediates seems to be not affected by LSPR, when taking the adsorption effect into account, we believe that LSPR effect still can promote the reaction rate of the main mono-hydroxylated intermediates.

Reference

1. M. R. Hoffmann, S. T. Martin, W. Y. Choi, D. W. Bahnemann, "Environmental applications of semiconductor photocatalysis", *Chemical Reviews*; **95**, 69-96 (1995).

2. A. Wold, "Photocatalytic properties of TiO_2", *Chemistry of Materials*; **5**, 280-283 (1993).

3. X. Chen, H. Y. Zhu, J. C. Zhao, Z. T. Zheng, X. P. Gao, "Visible-light-driven oxidation of organic contaminants in air with gold nanoparticle catalysts on oxide supports", *Angewandte Chemie-International Edition*; **47**, 5353-5356 (2008).

4. D. Li, W. J. Dong, S. M. Sun, Z. Shi, S. H. Feng, "Photocatalytic degradation of acid chrome blue k with porphyrin-sensitized TiO_2 under visible light", *Journal of Physical Chemistry C*; **112**, 14878-14882 (2008).

5. C. Yogi, K. Kojima, T. Takai, N. Wada, "Photocatalytic degradation of methylene blue by Au-deposited TiO_2 film under UV irradiation", *Journal of Materials Science*; **44**, 821-827 (2009).

6. T. Y. Wei, C. C. Wan, "Kinetics of photocatalytic oxidation of phenol on TiO_2 surface", *Journal of Photochemistry and Photobiology a-Chemistry*; **69**, 241-249 (1992).

7. A. Fujishima, K. Honda, "Electrochemical photolysis of water at a semiconductor electrode", *Nature*; **238**, 37-38 (1972).

8. O. M. Alfano, D. Bahnemann, A. E. Cassano, R. Dillert, R. Goslich, "Photocatalysis in water environments using artificial and solar light", *Catalysis Today*; **58**, 199-230 (2000).

9. A. G. Agrios, P. Pichat, "State of the art and perspectives on materials and applications of photocatalysis over TiO₂", *Journal of Applied Electrochemistry*; **35**, 655-663 (2005).

10. J. M. Herrmann, "Heterogeneous photocatalysis: State of the art and present applications", *Topics in Catalysis*; **34**, 49-65 (2005).

11. A. L. Linsebigler, G. Q. Lu, J. T. Yates, "Photocatalysis on TiO₂ surfaces: Principles, mechanisms, and selected results", *Chemical Reviews*; **95**, 735-758 (1995).

12. A. Fujishima, K. Hashimoto, T. Watanabe, "TiO₂ photocatalysis fundamentals and application", BKC, Inc. (1999).

13. "Phase diagrams for ceramists figure", The American Ceramic Society, Inc. 4150-4999 (1975).

14. U. Diebold, "The surface science of titanium dioxide", *Surface Science Reports*; **48**, 53-229 (2003).

15. A. Mills, S. Lehunte, "An overview of semiconductor photocatalysis", *Journal of Photochemistry and Photobiology a-Chemistry*; **108**, 1-35 (1997).

16. Y. Nosaka, M. A. Fox, "Kinetics for electron-transfer from laser-pulse-irradiated colloidal semiconductors to adsorbed methylviologen. Dependence of the quantum yield on incident pulse width", *Journal of Physical Chemistry*; **92**, 1893-1897 (1988).

17. J. M. Herrmann, "Heterogeneous photocatalysis: Fundamentals and applications to the removal of various types of aqueous pollutants", *Catalysis Today*; **53**, 115-129 (1999).

18. A. Hagfeldt, M. Gratzel, "Light-induced redox reactions in nanocrystalline systems", *Chemical Reviews*; **95**, 49-68 (1995).

19. E. Pelizzetti, C. Minero, V. Maurino, H. Hidaka, N. Serpone, R. Terzian, "Photocatalytic degradation of dodecane and of some dodecyl derivatives", *Annali Di Chimica*; **80**, 81-87 (1990).

20. L. M. Yang, L. E. Yu, M. B. Ray, "Photocatalytic oxidation of paracetamol: Dominant reactants, intermediates, and reaction mechanisms", *Environmental Science & Technology*; **43**, 460-465 (2009).

21. X. H. Huang, I. H. El-Sayed, W. Qian, M. A. El-Sayed, "Cancer cell imaging and photothermal therapy in the near-infrared region by using gold nanorods", *Journal of the American Chemical Society*; **128**, 2115-2120 (2006).

22. D. W. Chen, A. K. Ray, "Photodegradation kinetics of 4-nitrophenol in TiO$_2$ suspension", *Water Research*; **32**, 3223-3234 (1998).

23. K. Hofstadler, R. Bauer, S. Novalic, G. Heisler, "New reactor design for photocatalytic wastewater treatment with TiO$_2$ immobilized on fused-silica glass-fibers: Photomineralization of 4-chlorophenol", *Environmental Science & Technology*; **28**, 670-674 (1994).

24. A. Mills, S. Morris, "Photomineralization of 4-chlorophenol sensitized by titanium dioxide: A study of the initial kinetics of carbon dioxide photogeneration", *Journal of Photochemistry and Photobiology a-Chemistry*; **71**, 75-83 (1993).

25. G. Alsayyed, J. C. Doliveira, P. Pichat, "Semiconductor-sensitized photodegradation of 4-chlorophenol in water", *Journal of Photochemistry and Photobiology a-Chemistry*; **58**, 99-114 (1991).

26. L. C. Chen, T. C. Chou, "Kinetics of photodecolorization of methyl orange using titanium dioxide as catalyst", *Industrial & Engineering Chemistry Research*; **32**, 1520-1527 (1993).

27. M. C. Lu, G. D. Roam, J. N. Chen, C. P. Huang, "Factors affecting the photocatalytic degradation of dichlorvos over titanium dioxide supported on glass", *Journal of Photochemistry and Photobiology a-Chemistry*; **76**, 103-110 (1993).

28. Y. Inel, A. N. Okte, "Photocatalytic degradation of malonic acid in aqueous suspensions of titanium dioxide: An initial kinetic investigation of CO_2 photogeneration", *Journal of Photochemistry and Photobiology a-Chemistry*; **96**, 175-180 (1996).

29. K. Okamoto, Y. Yamamoto, H. Tanaka, A. Itaya, "Kinetics of heterogeneous photocatalytic decomposition of phenol over anatase TiO_2 powder", *Bulletin of the Chemical Society of Japan*; **58**, 2023-2028 (1985).

30. R. W. Matthews, "Photooxidation of organic impurities in water using thin films of titanium dioxide", *Journal of Physical Chemistry*; **91**, 3328-3333 (1987).

31. R. Terzian, N. Serpone, "Heterogeneous photocatalyzed oxidation of creosote components: Mineralization of xylenols by illuminated TiO_2 in oxygenated aqueous media", *Journal of Photochemistry and Photobiology a-Chemistry*; **89**, 163-175 (1995).

32. E. Hutter, J. H. Fendler, "Exploitation of localized surface plasmon resonance", *Advanced Materials*; **16**, 1685-1706 (2004).

33. K. Awazu, M. Fujimaki, C. Rockstuhl, J. Tominaga, H. Murakami, Y. Ohki, N. Yoshida, T. Watanabe, "A plasmonic photocatalyst consisting of sliver nanoparticles embedded in titanium dioxide", *Journal of the American Chemical Society*; **130**, 1676-1680 (2008).

34. M. Haruta, T. Kobayashi, H. Sano, N. Yamada, "Novel gold catalysts for the oxidation of carbon monoxide at a temperature far below $0°C$",

Chemistry Letters; 405-408 (1987).

35. M. Valden, X. Lai, D. W. Goodman, "Onset of catalytic activity of gold clusters on titania with the appearance of nonmetallic properties", *Science*; **281**, 1647-1650 (1998).

36. M. S. Chen, D. W. Goodman, "The structure of catalytically active gold on titania", *Science*; **306**, 252-255 (2004).

37. D. Vione, C. Minero, V. Maurino, A. E. Carlotti, T. Picatonotto, E. Pelizzetti, "Degradation of phenol and benzoic acid in the presence of a TiO$_2$-based heterogeneous photocatalyst", *Applied Catalysis B-Environmental*; **58**, 79-88 (2005).

38. B. Balamurugan, T. Maruyama, "Evidence of an enhanced interband absorption in Au nanoparticles: Size-dependent electronic structure and optical properties", *Applied Physics Letters*; **87**, (2005).

39. V. Augugliaro, L. Palmisano, A. Sclafani, C. Minero, E. Pelizzetti, "Photocatalytic degradation of phenol in aqueous titanium dioxide dispersions", *Toxicological and Environmental Chemistry*; **16**, 89-109 (1988).

40. C. G. Silva, J. L. Faria, "Effect of key operational parameters on the photocatalytic oxidation of phenol by nanocrystalline sol-gel TiO$_2$ under UV irradiation", *Journal of Molecular Catalysis a-Chemical*; **305**, 147-154 (2009).

Appendix A

The rate constants of 1,2-benzenediol and 1,4-benzenediol were fitted by our program written in Compaq Visual Fortran 6.5. We are going to illustrate the fitting steps with an example. The experimental conditions of the example are described as follows: The initial concentration is 150 ppm; the light source is UV light only; the catalyst is 2.0 wt% Au/P25; the reaction temperature is maintained at 318 K; the total reaction time is 360 minutes. The fitting equation shown below was derived from the simplified mechanism proposed by C. G. Silva et al. [40].

$$\frac{dC_1}{dt} = -kC_1 \text{ or } -k \tag{A-1}$$

$$\frac{dC_2}{dt} = k_1C_1 - k_3C_2 \tag{A-2}$$

$$\frac{dC_3}{dt} = k_2C_1 - k_4C_3 \tag{A-3}$$

I.C.: $C_1(0) = C_0$, $C_2(0) = 0$, $C_3(0) = 0$

$$\Rightarrow \begin{cases} C_1 = C_0 e^{-kt} \\ C_2 = e^{-k_3 t}\left[\frac{k_1 C_0}{k - k_3}\left(1 - e^{-(k-k_3)t}\right)\right] \\ C_3 = e^{-k_4 t}\left[\frac{k_2 C_0}{k - k_4}\left(1 - e^{-(k-k_4)t}\right)\right] \end{cases}$$

Because the concentration profile of phenol is less complicate than that of 1,2-benzenediol and 1,4-benzenediol, we fit C_1 with Eq. (A-1) first by applying commercial coverall software, such as Origin.

After we got k, we knew the ranges of k_1 and k_2, because theoretically, k_1+k_2 should be equal to k in order to satisfy the law of mass conservation. We then wrote do loops and substituted many sets of $k_1 \sim k_4$ into Eq. (A-2) and Eq. (A-3), combined with the known initial conditions, this set of ODE (Eq. (A-1)~(A-3)) can be solved. Although there exists analytical solutions of $C_1 \sim C_3$, which are listed below the fitting equations, we tried to apply 4th-order Runge-Kutta method to solve this set of ODE, because Runge-Kutta method can solve both linear and non-linear ODEs, which will allow us to modify the fitting equations further if there is a need.

Since that the kinetic model of phenol has been determined, the convergence criterion is judged by calculating the sum of the difference between the concentration of 1,2-benzenediol and 1,4-benzenediol obtained from the proposed model and experiment at the same time. Initially, we tuned the convergence criterion and the interval, not the range, of each k larger, say 0.1, trying to find out what is the range of each k that will lead to more sets of $k_1 \sim k_4$ to satisfy the convergence criterion. Then, we modified the ranges and intervals of do loops of $k_1 \sim k_4$, and run the program again. We would get more sets of $k_1 \sim k_4$, which could meet the convergence criterion, but it was difficult to pick out which combination of $k_1 \sim k_4$ could produce the least convergence criterion. The further step was to narrow the convergence criterion, and found out the set of $k_1 \sim k_4$ with the least corresponding sum of convergence. The simplified fitting steps are shown in Fig. A-1. Also, a part of the result of the fitting process is displayed in Table A-1, and the final fitting result is exhibited in Fig. A-2.
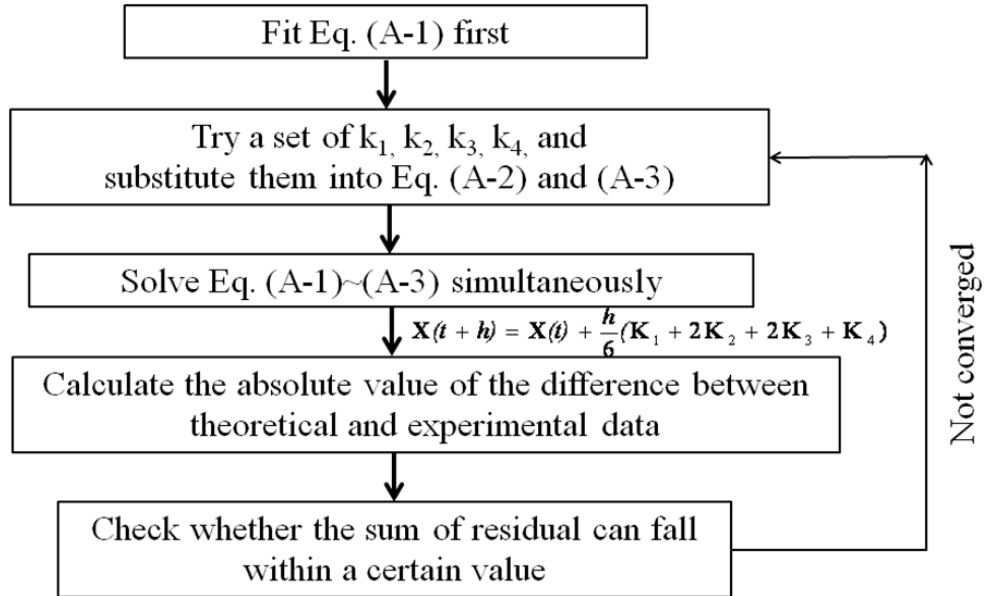
Fig. A-1. Flowchart of the fitting steps.

Table A-1. A part of the result of the fitting process.

k_1	k_2	k_3	k_4	Convergence criterion
6.00E-04	7.00E-04	3.00E-03	1.46E-02	2.92E-02
6.00E-04	7.00E-04	3.00E-03	1.48E-02	2.78E-02
6.00E-04	7.00E-04	3.00E-03	1.50E-02	2.74E-02
6.00E-04	7.00E-04	3.00E-03	1.52E-02	2.78E-02
6.00E-04	7.00E-04	3.00E-03	1.54E-02	2.86E-02
6.00E-04	7.00E-04	3.00E-03	1.56E-02	2.94E-02
6.00E-04	8.00E-04	2.80E-03	1.76E-02	2.95E-02
6.00E-04	8.00E-04	2.80E-03	1.78E-02	2.90E-02
6.00E-04	8.00E-04	2.80E-03	1.80E-02	2.85E-02
6.00E-04	8.00E-04	2.80E-03	1.82E-02	2.83E-02
6.00E-04	8.00E-04	2.80E-03	1.84E-02	2.91E-02
6.00E-04	8.00E-04	2.80E-03	1.86E-02	2.98E-02

6.00E-04	8.00E-04	3.00E-03	1.68E-02	2.89E-02
6.00E-04	8.00E-04	3.00E-03	1.70E-02	2.81E-02
6.00E-04	8.00E-04	3.00E-03	1.72E-02	2.76E-02
6.00E-04	8.00E-04	3.00E-03	1.74E-02	2.70E-02
6.00E-04	8.00E-04	3.00E-03	1.76E-02	2.65E-02
6.00E-04	8.00E-04	3.00E-03	1.78E-02	2.60E-02
6.00E-04	8.00E-04	3.00E-03	1.80E-02	2.55E-02
6.00E-04	8.00E-04	3.00E-03	1.82E-02	2.53E-02
6.00E-04	8.00E-04	3.00E-03	1.84E-02	2.61E-02
6.00E-04	8.00E-04	3.00E-03	1.86E-02	2.68E-02
6.00E-04	8.00E-04	3.00E-03	1.88E-02	2.76E-02
6.00E-04	8.00E-04	3.00E-03	1.90E-02	2.83E-02
6.00E-04	8.00E-04	3.00E-03	1.92E-02	2.91E-02
6.00E-04	8.00E-04	3.00E-03	1.94E-02	2.98E-02
6.00E-04	9.00E-04	3.00E-03	2.00E-02	2.97E-02
6.00E-04	9.00E-04	3.00E-03	2.02E-02	2.92E-02
6.00E-04	9.00E-04	3.00E-03	2.04E-02	2.87E-02
6.00E-04	9.00E-04	3.00E-03	2.06E-02	2.82E-02
6.00E-04	9.00E-04	3.00E-03	2.08E-02	2.78E-02
6.00E-04	9.00E-04	3.00E-03	2.10E-02	2.73E-02
6.00E-04	9.00E-04	3.00E-03	2.12E-02	2.75E-02
6.00E-04	9.00E-04	3.00E-03	2.14E-02	2.78E-02
6.00E-04	9.00E-04	3.00E-03	2.16E-02	2.81E-02
6.00E-04	9.00E-04	3.00E-03	2.18E-02	2.88E-02

|				
6.00E-04	9.00E-04	3.00E-03	2.20E-02	2.96E-02
6.00E-04	1.00E-03	3.00E-03	2.34E-02	3.00E-02
6.00E-04	1.00E-03	3.00E-03	2.36E-02	2.97E-02
6.00E-04	1.00E-03	3.00E-03	2.38E-02	2.97E-02
7.00E-04	7.00E-04	3.80E-03	1.42E-02	2.88E-02
7.00E-04	7.00E-04	3.80E-03	1.44E-02	2.74E-02
7.00E-04	7.00E-04	3.80E-03	1.46E-02	2.59E-02
7.00E-04	7.00E-04	3.80E-03	1.48E-02	2.46E-02
7.00E-04	**7.00E-04**	**3.80E-03**	**1.50E-02**	**2.42E-02**
7.00E-04	7.00E-04	3.80E-03	1.52E-02	2.46E-02
7.00E-04	7.00E-04	3.80E-03	1.54E-02	2.54E-02
7.00E-04	7.00E-04	3.80E-03	1.56E-02	2.62E-02
7.00E-04	7.00E-04	3.80E-03	1.58E-02	2.70E-02
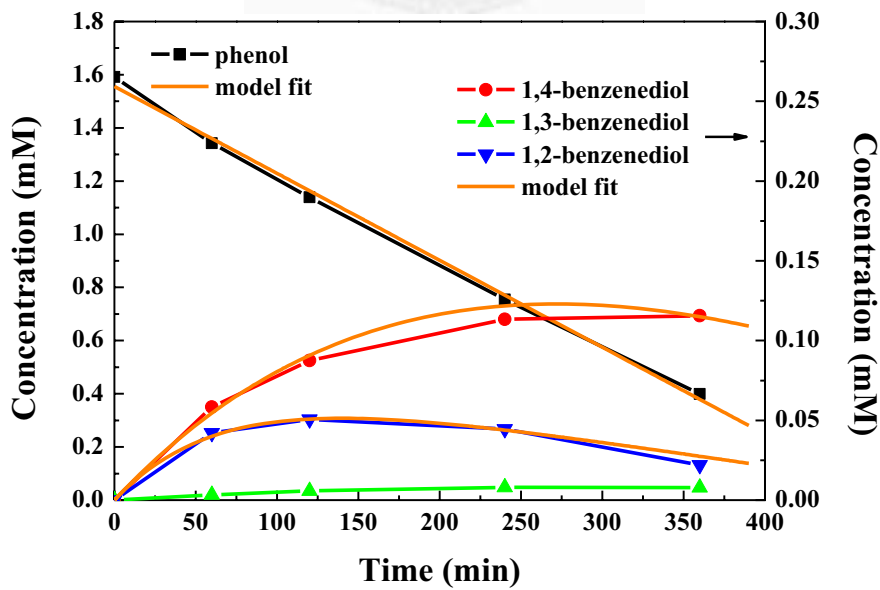
Fig. A-2. The final fitting result of the example.